

# **Bragg scattering of ultracold erbium atoms off a one-dimensional optical lattice potential**

David Helten

Masterarbeit in Physik  
angefertigt im Institut für Angewandte Physik

vorgelegt der  
Mathematisch-Naturwissenschaftlichen Fakultät  
der  
Rheinischen Friedrich-Wilhelms-Universität  
Bonn

November 2019

I hereby declare that this thesis was formulated by myself and that no sources or tools other than those cited were used.

Bonn, .....  
Date .....  
Signature

1. Gutachter: Prof. Dr. Martin Weitz
2. Gutachter: Prof. Dr. Simon Stellmer

# Contents

---

<b>1</b>	<b>Introduction</b>	<b>1</b>
<b>2</b>	<b>Bose-Einstein condensation of atomic erbium</b>	<b>3</b>
2.1	Bose-Einstein condensation . . . . .	3
2.2	Properties of atomic erbium . . . . .	5
2.3	Preparation of an erbium Bose-Einstein condensate . . . . .	7
2.3.1	Effusion cell . . . . .	8
2.3.2	Optical cooling . . . . .	9
2.3.3	Transverse cooling . . . . .	10
2.3.4	Zeeman slower . . . . .	11
2.3.5	Magneto-optical trap . . . . .	12
2.3.6	Dipole trap and evaporative cooling . . . . .	13
2.3.7	Absorption imaging . . . . .	14
2.3.8	Verification of the condensate state . . . . .	16
<b>3</b>	<b>Characterization of the 841 nm wavelength atomic erbium transition</b>	<b>17</b>
3.1	Theory of optical spectroscopy . . . . .	17
3.2	Set-up of the atomic beam spectroscopy . . . . .	19
<b>4</b>	<b>Diffraction of cold erbium atoms off a one-dimensional standing wave</b>	<b>23</b>
4.1	Optical lattice . . . . .	23
4.1.1	Diffraction on an optical lattice . . . . .	25
4.2	Experimental realization of an one-dimensional optical lattice potential . . . . .	28
4.3	Observation of a diffracted atomic erbium condensate . . . . .	32
<b>5</b>	<b>Conclusion and Outlook</b>	<b>37</b>
<b>Bibliography</b>		<b>39</b>
<b>List of Figures</b>		<b>45</b>
<b>List of Tables</b>		<b>47</b>
<b>Acronyms</b>		<b>49</b>



# CHAPTER 1

---

## Introduction

---

In 1924 N. S. Bose and A. Einstein presented the theoretical concept that in an ensemble of bosonic particles a macroscopic occupation of the energetic ground state appears at temperatures close to absolute zero [1–3]. This new state of matter, referred to as the Bose-Einstein condensate (BEC), offers the intriguing characteristic to be described by a single coherent one-particle wave function.

With the development of lasers and their application in laser cooling and trapping techniques for atoms in the second half of the 20th century, the first realization of such a condensate was achieved for different alkali metal by the groups of A. Cornell and C. E. Wieman for rubidium [4], W. Ketterle for sodium [5] and G. Hulet for lithium in 1995 [6]. With rising understanding of the underlying processes in the last two decades, it was possible to achieve condensate states for many other atomic species such as alkali earth metals like strontium [7], atoms with a more complex energy structure such as chromium [8] and even condensates at up to room temperatures using magnons [9], exiton-polaritons [10] and photons [11].

The very first experiments were performed using elements from the alkali metal group which are characterized by a simple hydrogen-like structure and an electronic ground state configuration with orbital angular momentum of  $L = 0$ . The vanishing angular momentum of the electronic ground state implies that e.g. Raman manipulation between ground state sublevels is only possible due to the additional fine and hyperfine structure, which limits the usable range of the detuning of the driving optical fields. This leads to an increase of the photon scattering rates and shorter coherence times for the BEC [12]. More recently the interest in condensation of atoms belonging to the group of lanthanide atoms has increased, with some of the corresponding atomic species having a non-vanishing electronic orbital angular momentum in the ground state. In addition, many of the corresponding atomic species have a large magnetic moment, giving rise to large dipole-dipole interactions. When using suitable electronic transitions, an electronic ground state configuration with non-vanishing orbital angular momentum should allow to overcome the mentioned lifetime limitations of alkali atoms in far detuned optical manipulation fields. Both dysprosium and erbium have a non vanishing orbital angular momentum ground state configuration and Bose-Einstein condensation has been achieved in both of these systems [13, 14].

While some experiments use the lanthanide properties to investigate the effects arising from strong dipole-dipole interactions [15, 16], this erbium experiment focuses on the possibility of state-dependent Raman manipulation with large detunings of the driving optical beams, arising from the non-vanishing

orbital angular momentum of  $L = 5$ . The Raman manipulation allows phase imprinting which can be used to create synthetic magnetic fields , possibly strong enough to observe fractional quantum Hall physics.

It has been pointed out that lanthanide atoms should allow the investigation of high synthetic magnetic fields via the phase imprinting method [17]. Synthetic magnetic fields, which manifest itself in observable vortex lattices structures in the condensates, have been produced by rotating field potentials that mimic a Lorentz and the Coriolis force in the neutral atoms [18, 19]. The magnitude of the generated synthetic field is with these schemes limited by the metastability of the rotated state. A different approach to generate synthetic gauge fields is to apply phase imprinting from Raman manipulation, which has already been demonstrated with rubidium atoms, but limited by the coherence times of the available transitions [20]. In comparison erbium with an orbital angular momentum of  $L = 5$  in the electronic ground state should allow for state-dependent Raman manipulation with large detunings that result in long coherence times and larger synthetic magnetic fields, giving rise to the possible investigation of fractional quantum Hall physics. Erbium with its rich energy structure offers several candidates for those Raman manipulations. As discussed in [21] the inner shell transition with an upper state electron configuration of  $4f^{11}(^4I_{15/2}^0)5d_{5/2}6s^2(15/2, 5/2)_7^0$  and  $J = 6 \rightarrow J' = 7$  at a wavelength near  $\lambda = 841$  nm has been found to be an attractive candidate.

A few years back the Bonn experiment has successfully demonstrated the worldwide second Erbium Bose-Einstein condensate [22]. While updating the experimental structures, the current aim is to realize synthetic magnetic fields in an Erbium condensate for the first time.

This thesis work focuses on the optical manipulation of erbium atoms on the atomic erbium inner shell transition near 841 nm wavelength. In a first part of the work, the spectra of this erbium transition were recorded for different isotopes in an atomic beam configuration. Subsequently, the optical structures for preparation of the Raman manipulating beams were set up and finally integrated at the main chamber. The transferred momentum of the observable first order diffraction configuration has been realized, and erbium atoms from a BEC were successfully diffracted of this standing wave tuned in the vicinity of the narrow-line transition.

In the following, chapter 2 describes the preparation of the cold erbium atomic sample and chapter 3 spectroscopic characterization measurements performed on the 841 nm wavelength transition. Chapter 4 then describes the diffraction of erbium condensate atoms of the one-dimensional standing wave, along with an analysis of signals and chapter 5 gives conclusions and an outlook.

# CHAPTER 2

---

## Bose-Einstein condensation of atomic erbium

---

The theoretical understanding of underlying concepts as well as the technical implementation of an erbium BEC condensate form necessary fundamentals for the subsequent tasks of implementing a spectroscopy and an optical lattice within the existing structure. The following chapter aims to briefly review the basics of Bose-Einstein condensation, the properties of atomic erbium to emphasize its extraordinary place within the periodic system and finally describe the different tools which are constituted in the Bonn experiment to create, control and observe the condensate.

### 2.1 Bose-Einstein condensation

In general quantum mechanical particles are divided into fermions and bosons, classified by their half-odd-integer-spin ( $S = 1/2, 3/2, \dots$ ) and integer spin ( $S = 1, 2, \dots$ ) respectively, where a particle of one sort is indistinguishable from the others of its kind. For fermions the wavefunction behaves anti-symmetric and for bosons symmetric under interchange of two particles. The anti-symmetric wavefunction gives rise to the Pauli exclusion principle, which prohibits that more than one fermion can occupy the same quantum state or in other words, that they cannot be characterized by the exact same quantum numbers [23]. This however does not hold for bosons where multiple particle can inhabit the same state. In 1924 S. N. Bose was the first who described an ideal Bose-gas of non interacting free photons, which can be considered as mass-less bosons. A. Einstein then expanded Booses idea onto massive bosons [2].Bose-Einstein statistics describes the mean occupation number for a state  $\nu$  with energy  $\epsilon_\nu$  as

$$f(\epsilon_\nu) = \frac{1}{e^{(\epsilon_\nu - \mu)/k_B T} - 1} \quad (2.1)$$

for a system of non interacting particles in thermal equilibrium with temperature  $T$ , chemical potential  $\mu$  and Boltzmann constant  $k_B$  [24].

The chemical potential is a function of the total number of particles  $N$  and the temperature, where the total number of particles has to be conserved and is equal to the sum over the atoms in all energy states. Since the chemical potential decreases for rising temperatures and thus  $|\mu| \ll k_B T$  the distribution will follow classical Boltzman statistics for high temperatures

$$f(\epsilon_\nu) \simeq e^{-(\epsilon_\nu - \mu)/k_B T} \quad (2.2)$$

where quantum statistic becomes negligible and the mean occupation number of a single state is much smaller than one.

For falling temperatures the chemical potential rises. However it can not exceed the ground state energy  $\mu = \epsilon_0$  since otherwise the function eq. (2.1) would become negative, which corresponds to an unphysical solution. Followed by that, the number of atoms in the excited state must be limited and more than one atom can occupy the ground state which has no occupation limit.

From atom number conservation the total number of atoms follows as sum of exited and ground state atoms:

$$N = N_0 + N_{\text{ex}} = N_0 + \int_0^{\infty} g(\epsilon) \cdot f(\epsilon) \, d\epsilon \quad (2.3)$$

where the number of excited states can be gained by integrating the density of states  $g(\epsilon)$  over all energies. The phase transition between the thermal and the condensate state of an ensemble of atoms is indicated by the critical temperature  $T_C$  and indicates the highest temperature for which a macroscopic occupation of the ground state appears.  $T_C$  can be derived by assuming  $\mu = 0$  for which  $N_{\text{ex}}$  becomes maximal and calculates to [24]

$$N_{\text{ex}}(T_C, \mu = 0) = \int_0^{\infty} g(\epsilon) \frac{1}{e^{\epsilon/k_B T_C} - 1} \, d\epsilon \quad . \quad (2.4)$$

The density of states scales as a power of energy, where the exponent depends on the dimension of the potential which confines the atomic ensemble. Evaluation of  $T_C$  can then be performed using gamma and Riemann zeta functions for different potential shapes as shown in [24].

It is useful to define the so called phase-space density which expresses the number of particles which are confined in the volume of a cube with edge length equal to the de Broglie wavelength  $\lambda_{\text{dB}} = \sqrt{2\pi\hbar^2/(mk_B T)}$ :

$$\rho = n\lambda_{\text{dB}}^3 = n \left( \frac{2\pi\hbar^2}{\sqrt{mk_B T}} \right)^{3/2} \quad (2.5)$$

with  $n = N/V$  being the number density and  $m$  the mass. For the approximation of a gas in a three-dimensional box-potential the critical temperature reads as

$$T_C \approx 3.31 \frac{\hbar^2 n^{2/3}}{m} \quad (2.6)$$

By inserting eq. (2.6) into eq. (2.5) the necessary phase space density for a three dimensional box potential at which Bose-Einstein condensation occurs follows as  $\rho_C \geq 2.612$ . Referring to particle-wave duality which manifests in the de Broglie wavelength by assigning a wavelength to every individual massive particle, this process can be thought of as an overlap of their wave functions which increase with lowering temperatures until the ensemble in a confined phase space can be described by a single wave packet. A detailed introduction on the behavior of Bose-Einstein condensation trapped gases can be found in [24] and [25].

## 2.2 Properties of atomic erbium

Erbium is a rare earth element with the atomic number 68 and belongs to the series of Lanthanide atoms. It was first discovered in 1843 by G. Monsander, who though to have found a pure erbium-oxide, which was in reality a mixture of different rare earth metal oxide [26, 27]. Pure atomic erbium was successfully isolated in 1934 by W. Klemm and H. Brommer [28]. Under standard conditions it appears as solid with a silver shining surface, which oxidizes when in contact with air. With a melting point of 1 802 K and boiling point of 3 136 K the solid erbium metal needs to be heated to high temperatures to evaporate to a free atomic gas which can be used for the here discussed experimental purposes [29].

Nowadays erbium is widely used in commercial application such as doped Silicon fibres which are used in fibre amplifiers well suited for laser amplification of the standard telecommunication wavelength 1 530 nm [30].

As listed in table 2.1 erbium has six stable isotopes, from which, according to their nuclear spin, five are of bosonic and one is of fermionic nature. For this experiment the  $^{168}\text{Er}$  isotope is chosen, due to its high relative abundance of 26.8 %, bosonic nature and preferable scattering properties. In comparison to other, in cold atom physics commonly used alkali atoms (i.e. rubidium, caesium), erbium offers a high magnetic moment of seven Bohr magneton  $7\mu_B$ , where  $\mu_B$  denotes the Bohr magneton [31]. Furthermore erbium atoms features a rather complicated energy level structure which results from an open  $4f$  shell. An illustration of the level scheme is shown in fig. 2.1. Due to that erbium offers an angular momentum of  $L = 5$  in the electronic ground state which can be depicted as  $[\text{Xe}]4f^126s^2$ . This non-vanishing angular momentum of the ground state allows for optical manipulation in the gross structure. Meaning that the detuning of optical beams for state-dependent Raman manipulation can be chosen much greater as for example in alkali atoms and leads to longer coherence times and potential stronger synthetic gauge fields [17].

For this experiment the transitions near 401 nm, 583 nm and 841 nm are selected for certain applications in the experimental cycle. A collection of characteristic values resulting from the different line-widths can be found in table 2.2. There specific application within the experiment will be discussed in detail in the following chapter.

Isotope	Abundance / %	Atomic mass / u	Nuclear Spin / $\hbar$
$\text{Er}^{162}$	0.14	161.929	0
$\text{Er}^{164}$	1.61	163.929	0
$\text{Er}^{166}$	33.6	165.930	0
$\text{Er}^{167}$	22.95	166.932	7/2
<b><math>\text{Er}^{168}</math></b>	<b>26.8</b>	<b>167.932</b>	<b>0</b>
$\text{Er}^{170}$	14.9	169.935	0

Table 2.1: Listed are all six stable atomic erbium isotopes with their relative abundance, mass and isospin. All bosons have a nuclear spin of zero and only the  $\text{Er}^{167}$  is of fermionic particle type [32]. The in this experiment used isotope is highlighted in bold.

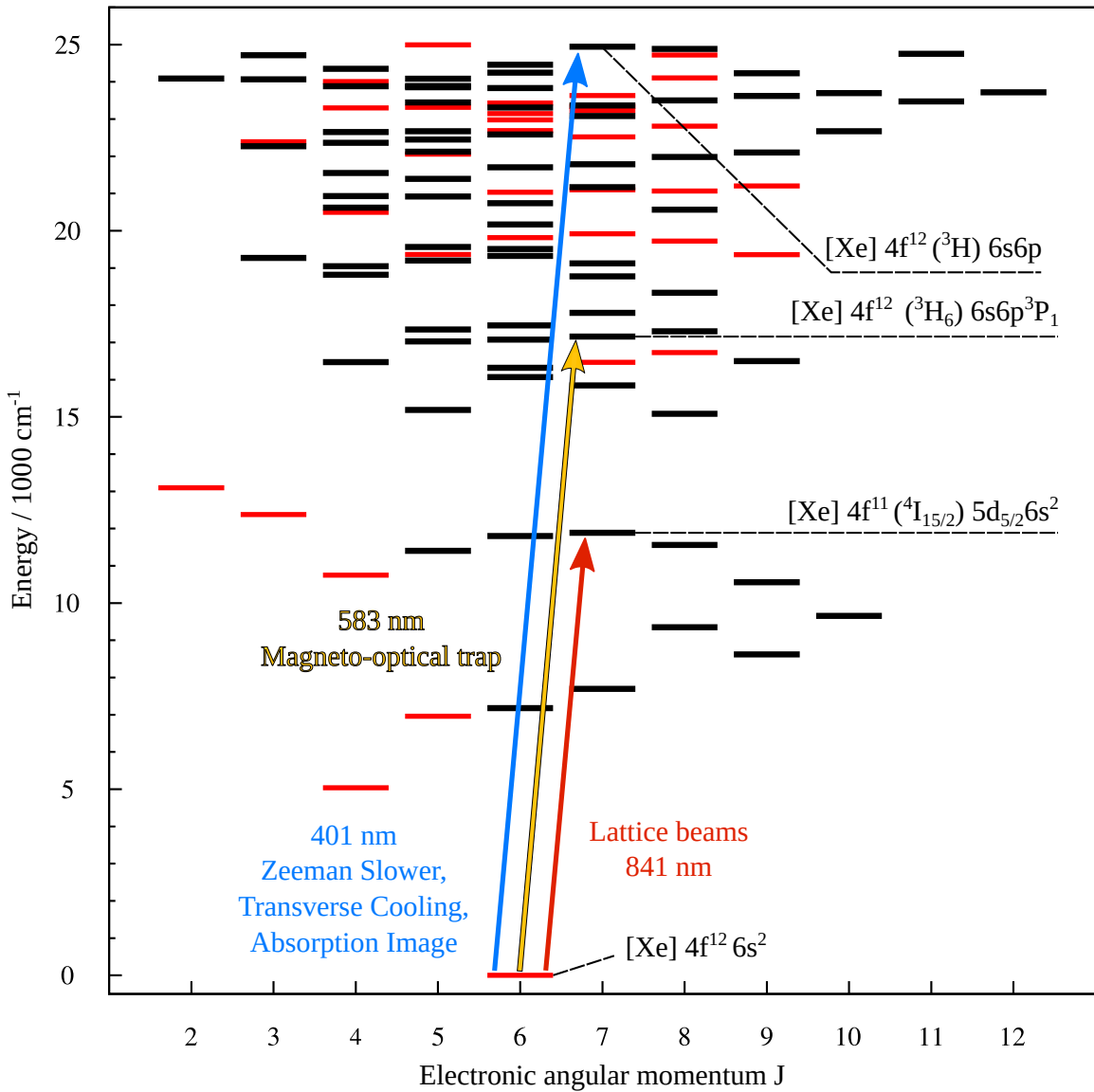


Figure 2.1: Energy level scheme for atomic erbium in dependence of the total angular momentum  $J$  up to a energy relevant for this experiment. Levels marked in black are of odd, those marked in red of even parity. The transitions used in this experiments are marked by colored arrows. [Xe] abbreviates the full electron configuration with the related noble gas Xenon. Spectroscopy data taken from NIST [31].

### 2.3 Preparation of an erbium Bose-Einstein condensate

---

Wavelength		400.796 nm	582.681 nm	841.990 nm
Exited state		$4f^{12} ({}^2H) 6s6p$	$4f^{12} ({}^3H_6) 6s6p {}^3P_1$	$4f^{12} (I_{15/2}) 5d_{5/2} 6s^2$
Lifetime	$\tau$	4.5 ns	857 ns	20 $\mu$ s
Natural linewidth	$\Delta\nu_{\text{nat}}$	33.37 MHz	185.71 kHz	7.96 kHz
Decay rate	$\gamma$	$2.22 \times 10^8 \text{ s}^{-1}$	$1.17 \times 10^6 \text{ s}^{-1}$	$50.00 \times 10^3 \text{ s}^{-1}$
Saturation Intensity	$I_{\text{sat}}$	71.80 mW cm $^{-2}$	0.12 mW cm $^{-2}$	1.74 $\mu$ W cm $^{-2}$
Doppler temperature	$T_{\text{Doppler}}$	848.69 $\mu$ K	4.46 $\mu$ K	0.19 $\mu$ K
Doppler velocity	$v_{\text{Doppler}}$	20.50 cm s $^{-1}$	1.49 cm s $^{-1}$	0.31 cm s $^{-1}$
Recoil temperature	$T_{\text{Recoil}}$	354.95 nK	167.94 nK	80.43 nK
Recoil velocity	$v_{\text{Recoil}}$	5.93 mm s $^{-1}$	4.08 mm s $^{-1}$	2.82 mm s $^{-1}$

Table 2.2: Collection of characteristic values for the used transitions in atomic erbium. Literature values for the transition lifetimes are taken from [33–36]. For relations between some of these values please see section 3.1.

## 2.3 Preparation of an erbium Bose-Einstein condensate

The preparation of the erbium condensate requires an interplay of several experimental stages, based on the foundation of different physical principles.

This chapter briefly introduces the necessary steps and shall give a basic idea of the underlying physical concepts. A more detailed description can be found in the PhD thesis of J. Ulitzsch [37] and the corresponding previous works which have covered the respective implementation of each.

An overview of the set-up can be found in fig. 2.2. The lasers which are used to generate resonant light are placed on different optical tables to prevent any stray light from reaching the main chamber during the sensitive dipole-trap phase of the experiment. From there, the light is guided using optical fibers to the desired place at the main experiment and can be shuttered mechanical (slow) and with acousto-optic modulators(fast) before entering the fiber.

The whole experiment is kept in an ultra high vacuum, since collisions with non cooled erbium atoms or any other room temperature gases would lead to destructive-heating effect on the trapped atomic cloud. The vacuum is maintained by an ion gutter pump to reach a pressure of about  $10^{-8}$  mbar for the oven and Zeeman slower stage and an additional titan sublimation pump at the main chamber to pump down to  $10^{-10}$  mbar. The manipulating laser beams are entering the vacuum through several viewports of different sizes and coatings optimized for the specific optical wavelength on their axis. All experimental processes, such as tuning the intensity of magnetic fields and lasers, have to happen in a precise chronological sequence. The experimental properties can be tuned by a *Python* based software that transmits over 40 parameters to the real time system *ADwin-Pro II* from the company *Jäger* which offers several digital and analogue outputs for electronic triggering and tuning.

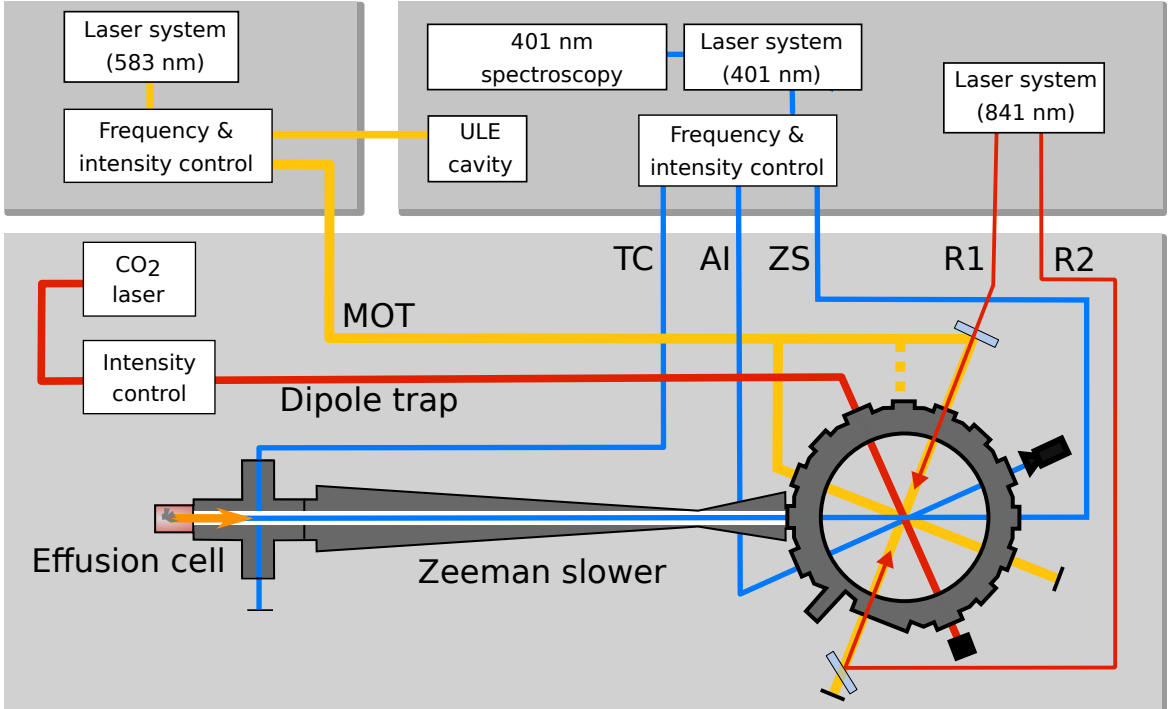


Figure 2.2: Schematic overview of the whole experimental set-up. The different optical tables are indicated by a gray background. The yellow laser beam is used for the magneto-optical trap (MOT). The yellow dotted line indicates the MOT beam on vertical axes. Laser source is a rhodamine dye laser system, which is frequency locked to an ultra low expansion cavity (ULE cavity). The blue laser beams are used for the transverse cooling (TC), absorption image (AI) and Zeeman slower (ZS). The beam is generated by a frequency doubled diode laser, locked to a spectroscopy signal of the  $^{168}\text{Er}$  transition near 401 nm using the modulation transfer spectroscopy technique in a hollow cathode lamp. R1 and R2 indicate the two lattice beams, detuned from the 841 nm transition and generated with a Ti:Sapphire laser system.

### 2.3.1 Effusion cell

To gain a gas of atomic of erbium atoms, an effusion cell separated into two stages is used. As shown in fig. 2.3 the solid erbium is placed in the first part of a tantalum crucible called *effusion cell* (EC) which gets heated by a current running through tantalum wire up to  $1\,200\text{ }^\circ\text{C}$ . With the aim to achieve a rather directed beam of atoms, the EC has a pinhole of 3 mm diameter followed by a second inlet with another pinhole of 3 mm. To prevent the erbium atoms from condensing at the pinholes and thus possibly clogging the opening the second stage, called *hot lip* (HL) is heated to a higher temperature of  $1\,400\text{ }^\circ\text{C}$ . Even though this set-up is intended to produce a rather focused beam with less transverse velocity and reduced evaporative pressure in the HL, measurements by J. Schindler from Innsbruck [38], which use a similar set-up in place, showed that the evaporative pressure is mainly the same in both regions and the collimating effect by the two pin holes is not dominating.

An estimation of the root mean squared (RMS) velocity of the atoms leaving the oven can be derived from the average energy of the particle in an ideal gas [39]:

$$\bar{v} = \sqrt{\frac{3k_B T}{m}} . \quad (2.7)$$

Resulting in  $\bar{v}_{EC} \approx 500 \text{ m s}^{-1}$  for a HL temperature of 1 673 K. To prevent atoms from destructing the sensitive trapped atomic ensemble during the later following dipole trap phase, a mechanical shutter is installed after the oven which blocks the atomic flow after the magneto-optical trap is loaded with atoms.

### 2.3.2 Optical cooling

As seen from eq. (2.7), the temperature of an ideal gas is proportional to its mean velocity, thus a deceleration of the atoms will result in a reduced temperature. To achieve a reduction in velocity, a technique called optical or laser cooling is commonly used and is based upon the force photons can apply onto particles by transferring their momentum, also related to as radiation pressure.

Following [40] this process can be described by considering the atom as a two level system. This system has a ground state  $|g\rangle$  and an excited state  $|e\rangle$  with an energy difference of  $\Delta E = \hbar\omega_0$ , which is related to the resonance frequency  $\omega_0$ . By absorbing a photon with correct frequency, the atom at rest can be transferred from the ground to the excited state absorbing the photon energy. During this process the atom also takes the initial momentum  $\vec{p} = \hbar\vec{k}$  of the photon, which's magnitude only depends on the wavevector  $\vec{k}$  that is correlated to the wavelength  $\lambda$  of the used light via  $k = 2\pi/\lambda$ . The atom can relax from the excited state either by stimulated or spontaneous emission. For stimulated emission a photon triggers the relaxation of the atom, resulting in a second photon with the same frequency, phase and direction as the stimulating one. To obey momentum conservation the atom receives a momentum opposite to the direction of the emitted photon. If assumed that all photons come from a primary direction, like it is the case for a laser beam, the atoms do not gain an effective momentum transfer by this process since it adds up to zero with the absorption. In the case of spontaneous emission however, a photon is emitted in a random direction after the decay time  $\tau = 1/\gamma$ , where  $\gamma$  represents the decay rate. Since this emission is isotropic in all spatial directions the corresponding momentum transfer by the relaxation process is isotropic as well and adds up to zero, resulting in an effective momentum transfer in the direction of the incoming photon.

By solving the optical Bloch equations for an atom at rest, a solution for the population of the excited state can be obtained, which reads

$$\rho_{ee} = \frac{s_0/2}{1 + s_0 + (2\delta/\gamma)^2} . \quad (2.8)$$

Here  $\delta = \omega - \omega_0$  marks the detuning of the laser frequency  $\omega$  from the resonance frequency. The on-resonance saturation parameter  $s_0 = I/I_s$  depends on the used excitation intensity  $I$  as well as on the saturation intensity

$$I_s = \frac{\pi h c \gamma}{3\lambda^3} . \quad (2.9)$$

The force acting on the atom by absorption process is described by

$$\vec{F} = \hbar \vec{k} \gamma \rho_{ee} = \frac{\hbar \vec{k}}{2} \frac{s_0 \gamma}{1 + s_0 + (2\delta/\gamma)^2} \quad (2.10)$$

where the definition from eq. (2.8) is inserted and the direction of the wavevector  $\vec{k}$  marks the direction of the force.

It is necessary to consider the Doppler shift which arises from the relative velocities between the inertial systems of photons and atoms. The atoms experience a shifted frequency  $\Delta\omega_{\text{Doppler}} = -\vec{k}\vec{v}$  where  $\vec{v}$  marks the velocity of the atom. Including this into eq. (2.10) gives:

$$\vec{F} = \frac{\hbar \vec{k} \gamma}{2} \frac{s_0}{1 + s_0 + \left(\frac{2(\delta - \vec{k}\vec{v})}{\gamma}\right)^2} \quad (2.11)$$

By using a red-detuned laser, for which  $\delta < 0$ , that propagates opposite to the atomic movement, the atoms will get slowed down in this direction and thus lower their temperature. However, there is a limit to the cooling effect resulting from the fact that the mean squared value of the momentum transfer does not vanish, even though the effective momentum sums up to zero after several absorption and emission processes. This heating effect leads to an equilibrium state where it is equal to the cooling rate, resulting in the so called Doppler temperature:

$$T_D = \frac{\hbar \gamma}{2k_B} \quad (2.12)$$

This characteristic temperature, sometimes also referred to as the *Doppler limit*, is given by the decay rate  $\gamma$  of the used atomic transition [40]. The decay rate is connected to the natural line-width via  $\gamma = 2\pi\Delta\nu_{\text{nat}}$ . From eq. (2.10) and eq. (2.12) a trade-off between strong deceleration from a high force achieved by choosing a large decay rate and low Doppler temperatures for small decay rates arises. By using more elaborated techniques, e.g. polarization gradient cooling, it is possible to reach temperatures below the Doppler limit [41]. Different from the previous consideration of a pure two level system, it is possible that the excited state partially decays into intermediate states before decaying into the ground state, which effectively reduces the radiative pressure for the time being in this dark state. If an intermediate state has a relatively long lifetime, a so called dark state, the atoms will not be effected by any cooling and one has to consider another pump laser to deplete those levels. The identification of a proper, preferably closed, transition with no intermediate states is thus inevitable to reach the desired effects.

### 2.3.3 Transverse cooling

As illustrated in fig. 2.3 the opening angle of the atomic beam leaving the effusion cell limits the number of atoms which successfully enter the narrow tube of the Zeeman slower. Thereby it acts as a third aperture, defining the final radius of the atomic beam that reaches the main chamber. In order to increase the atomic flux, the atomic beam is collimated by a transverse cooling set-up. As illustrated in fig. 2.3 it consists of a laser impinging transverse on the atomic beam from four perpendicular directions. Optical cooling is achieved using the red-detuned 401 nm transition. The wide natural

line-width of 33.37 MHz allows to address different transverse velocity components and, followed by eq. (2.11), a large radiation pressure which acts towards the center of the atomic beam. To increase the effective cross section, the beam is enlarged to an elliptical shape, with its longer semi-axis lying parallel to the beam propagation. Parameters as power, detuning and beam alignment are optimized by maximizing the atomic number in the later introduced magneto-optical trap (MOT) and generally lead to an increase in atom number by a factor of two to four. Details on the characterization of this set-up can be found in [37]. A theoretical background on transverse cooling can be obtained from [42].

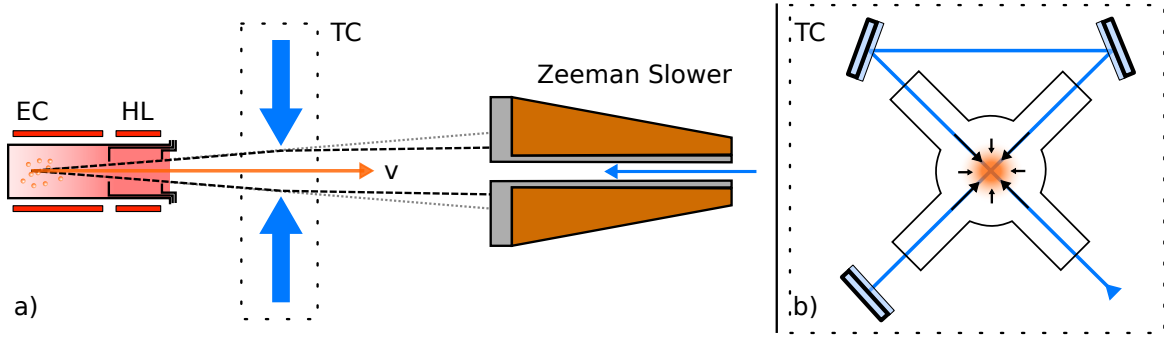


Figure 2.3: a) Illustration of the effusion cell with its two apertures. Side view onto the transverse cooling stage and the beginning of the Zeeman slower. b) shows the cross section through the Zeeman slower, indicating the radiative pressure acting from four directions to collimate the diverging atomic beam.

#### 2.3.4 Zeeman slower

With a longitudinal velocity of about  $500 \text{ m s}^{-1}$  the atoms are too fast to be trapped by the MOT, which has a maximal capture velocity of a few meters per second [37]. To decelerate the atoms, a Zeeman slower is used, which has been developed and is described in detail in a previous thesis [43]. Again the effect of optical cooling is used by introducing a red-detuned laser beam of 401 nm counter propagating to the atomic beam direction. As introduced in section 2.3.2 the laser light has to be resonant with the moving atoms in order to achieve the highest radiative pressure. Since the resonance condition changes for different velocities due to the Doppler shift, a counter propagating laser beam which has a fixed wavelength would only address a certain velocity group and would not have the effect of a continuous deceleration. To overcome this, the Zeeman slower consists of water cooled magnetic coils with decreasing winding number along the direction of atomic movement, that produce a position-dependent magnetic field. This leads to a position-dependent energy shift of the atomic level, referred to as *Zeeman splitting* which scales with

$$\Delta\omega_Z = \frac{\mu_{\text{eff}}}{\hbar} |\vec{B}| \quad (2.13)$$

where  $\mu_{\text{eff}}$  indicates the effective magnetic moment and  $|\vec{B}|$  the modulus of the magnetic field [40]. To achieve a permanent deceleration over the whole Zeemann slower tube, the Doppler frequency shift  $\Delta\omega_D = -k\vec{v}$  must match  $\Delta\omega_Z$  and is achieved by a carefully designed winding structure. The here implemented device is a spin-flip Zeeman slower which introduces a zero-crossing of the magnetic field along the propagation axis to take care of the spin flip which arises during deceleration with a

red-detuned laser beam. This has the advantage of achieving the same deceleration as with a higher maximal magnetic field, which needs higher currents (see [43]for more details).

### 2.3.5 Magneto-optical trap

Directly after the Zeeman slower the atoms enter the main chamber. It offers 17 ports of different diameter through which the lasers can enter via anti-reflection coated windows. The atoms reaching the main chamber are slowed down to a few meters per second, but are not confined locally in space. This is achieved by using a MOT, introducing a three dimensional spatially dependent restoring force. Based on the principles of optical cooling, two counter propagating laser beams, red detuned the 583 nm transition with a diameter of approximately four centimeter, for each of the three spatial dimensions, intercept in the middle of the chamber creating a optical molasses. Two water cooled coils in anti-Helmholtz configuration, under and above the chamber, create a magnetic quadrupole field, which is tuned such that it has its zero point at the crossing point of the six laser beams. Additional six offset coils in Helmholtz configuration allow for precise spatial tuning of the magnetic field and compensation of the earth magnetic field. When considering the atom as a two level system, the ground state with  $J = 0$  has only one possible Zeemans state  $m_J = 0$ , while the excited state with  $J' = 1$  splits up into three states with  $m_J = [0, \pm 1]$ . The quadrupole field splits up the degeneracy of the states depending on the local position of the atoms as illustrated in fig. 2.4. Due to momentum conservation, the  $m_J = +1$  transitions are only addressed by right-circular polarized light ( $\sigma^+$ ) and the  $m_J = -1$  only by left-circular polarized ( $\sigma^-$ ). The combination of these effects leads to a direction dependent restoring force for atoms that moves away from the center of the MOT. Due to the narrow line-width of 186 kHz of the chosen transition, the here implemented MOT is referred to as a narrow-line MOT, allowing for lower temperatures in the MOT (compare eq. (2.12)). In the experimental cycle the MOT changes from a loading phase, where it collects the atoms from the Zeeman slower, to a compressed phase. During the loading phase the Zeeman slower passes over the atoms and is switched off for the compressing. This is achieved by detuning of the laser and magnetic fields whereby the atomic cloud is confined into a denser an more localized state.

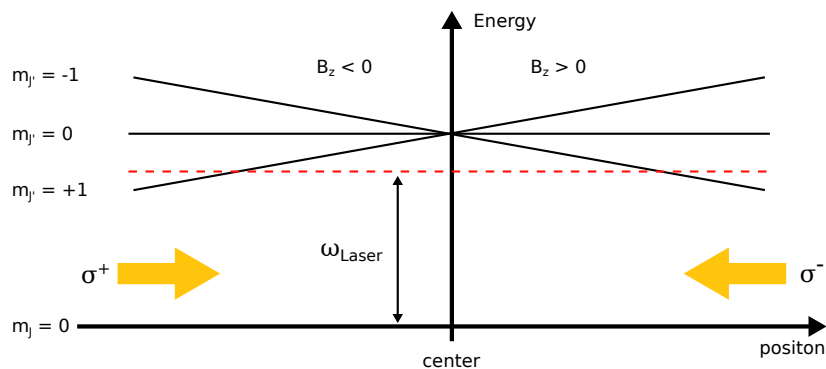


Figure 2.4: Energy scheme for a  $J = 0 \rightarrow J' = 1$  transition. Here shown is an exemplary cut through the z-axis of the three dimensional quadrupole magnetic field. The different circularly polarized beams do only interact with atoms moving towards them and away from the center of the trap. The dashed red line indicates the relative to the 583 nm red-detuned transition of the yellow laser. Adapted figure from [40].

Typical experimentally achieved parameters for the MOT are temperatures of about 20 µK for about 100 million atoms which are confined in a radius of approximately 130 µm. A comprehensive description of the working principles of magneto-optical traps can be found in [40]. For a characterization of the here implemented set-up please refer to [37, 44].

### 2.3.6 Dipole trap and evaporative cooling

As the atoms are confined in the MOT, the lowest achievable temperature with this technique is low enough to not reach the in section 2.1 introduced critical temperature  $T_C$  which is necessary to achieve Bose-Einstein condensation. To reach lower temperatures, the atoms are transferred into an optical dipole trap (ODT) that consists of a CO<sub>2</sub>-laser beam near a wavelength of 10.6 µm with a maximal power of approximately 63 W focused to a radius of about 25 µm inside the main chamber. Due to the wavelength of the trap and its far detuning from any erbium transition, the implemented trap can be approximated as a quasi-electrostatic trap [37].

A great introduction into the working principles of optical dipole traps for neutral atoms can be found in the review paper of R. Grimm and M. Weidemüller [12]. For a good overview of *Bose-Einstein condensation in trapped gases* in general, the review paper by F. Dalfovo and S. Giorgini [25] is recommended. Referring to this literature, it is intended to give a brief overview in the following, as the topic is also related to the physical effects of optical lattices.

The ODT is based on the induction of an atomic dipole moment in an atom which is placed in the electric field  $\vec{E}(\vec{r})$  of a laser and scales linearly with the frequency dependent complex polarisability  $\alpha(\omega)$  as  $p(\vec{r}) = \alpha(\omega) \cdot \vec{E}(\vec{r})$ . The dipole in the oscillating field then results in an interaction potential

$$U_{\text{dip}} = -\text{Re}(\alpha) \frac{I(\vec{r})}{2\epsilon_0 c} \quad (2.14)$$

where  $I(\vec{r})$  corresponds to the laser intensity which in turn is related to the electric field via  $I = 2\epsilon_0 c |\vec{E}|^2$  with the Vacuum permittivity  $\epsilon_0$  and the speed of light  $c$ . As the intensity of the used lasers can be described by the distribution of a Gaussian beam profile represented in cylindrical coordinates by

$$I(r, z) = \frac{2P}{\pi w^2(z)} e^{-2r^2/w^2(z)} \quad (2.15)$$

with  $w$  the beam radius,  $P$  the total laser power and  $r$  the radial position along the  $z$ -axis of the propagation. From there a locally dependent potential

$$U_{\text{dip}}(r, z) = -U_0 e^{-2r^2/w^2(z)} \quad (2.16)$$

with the highest intensity at the position  $U_0 = -U_{\text{dip}}(r = 0, z = 0) = \frac{\text{Re}(\alpha)P}{\epsilon_0 c \pi w_0^2}$  follows for a beam waist of  $w_0 = w(0)$ . Considering a dilute gas which has a thermal energy  $k_B T$  much smaller than the potential depth, its radial and longitudinal expansion can be assumed to be smaller than the beam waist  $w_0$  and the Rayleigh length  $z_R = \pi w_0^2/\lambda$  respectively. This allows to approximate the trap by a cylindrical

symmetric harmonic oscillator potential following from a Taylor expansion of  $U_{\text{dip}}$  around  $r, z = 0$ :

$$U_{\text{harm}} = -U_0 \left[ 1 - 2 \left( \frac{r}{w_0} \right)^2 - \left( \frac{z}{z_R} \right)^2 \right] \quad (2.17)$$

The harmonic potential is characterized by its radial and longitudinal trap frequencies  $\omega_r = \sqrt{4U_0/mw_0^2}$  and  $w_z = \sqrt{2U_0\lambda^2/m\pi^2 w_0^4}$ , that describe the oscillations of the atomic ensemble within the trap.

### Evaporative cooling

The ODT itself being a conservative trap does not allow any further cooling of the atoms and scaling with the photon scattering rate even heats up the atoms. The here used quasi-electrostatic trap however has a large red-detuning and thus a low scattering rate. Nevertheless, in order to achieve further cooling the technique of *evaporative cooling* first introduced in 1988 is used [45]. As the velocity distribution of the trapped atoms follows a Maxwell-Boltzmann distribution with a mean velocity  $\bar{v}$ , there are atoms with a higher velocity corresponding to atoms with higher energy than others. If these atoms are removed from the trap, a reduction of the average velocity and thus a lower gas temperature follows. This is done by lowering the laser power. The most energetic atoms can escape the trap which leads to a cut-off at the tail of the Boltzmann distribution and after a sufficient time the Maxwell-Boltzman distribution is restored in a re-thermalization process via interatomic collisions. This process is done in a continuous ramp which needs to have a specific shape. Too fast ramping does not allow for sufficient re-thermalization and thus no temperature reduction. For too slow ramping on the other hand the heating effects in the system can dominate, resulting in a loss of atoms before any sufficient cooling has been possible. A theoretical description of the requirements for the time varying potential can be obtained from [46]. Characterizing measurements of the implemented trap and evaporative cooling cycle have been performed in previous theses by R. Röll and J. Ulitzsch. They specify a typical condensate state with 30 000 atoms and temperatures below 200 nK [37, 44].

### 2.3.7 Absorption imaging

To observe the consequences of experimental adjustments and gain analyzable data an absorption imaging system is used. A short pulse ( $80 \mu\text{s}$ ) of resonant 401 nm light is shot onto the atomic cloud. Opposite to the flash source, a lens with focal length of  $f = 200 \text{ mm}$  in a distance of  $(260 \pm 20) \text{ mm}$  to the atomic cloud, projects the light onto a CCD-camera. The resolution of the imaging system is limited as  $(4 \pm 1) \mu\text{m}$  [37]. Because the cloud of atoms absorbs the resonant light, but reemits it incoherently and isotropic, the produced image shows a shadow at the positions of the cloud, where the intensity of the shadow scales with the density of the cloud. A second picture with the flash beam on is taken after the atomic cloud has been dispersed. By subtracting the background, taken in a third picture with no flash on, from both images and then dividing them, the absorption picture is generated. An implementation of the Lambert-Beer law is used to calculate the number of atoms, which is one of the measured physical values [37]. Since the cloud of confined atoms is destroyed by the resonant light, the measurement is irreversible and to probe different parameters for their effects, the experimental cycle has to be repeated several times. Other extractable parameters are the distribution and position

of atoms on the image. To convert the position in pixels into a actual distance in meters, a calibration measurement of the imaging system is necessary. Since any conclusions resulting from the distance of the in section 4.3 introduced splitting of the atomic cloud depends critically on the magnification factor, a new calibration was performed. This was done by releasing cold atomic ensembles from the trap and observing their position for different time of flight (TOF) duration. Because the atoms are accelerated by the gravitational field of the earth, it is possible to compare the fit results of a simple equation of motion

$$y(t) = \frac{1}{2}g_{\text{fit}}t^2 + b \quad (2.18)$$

to the known value for the acceleration in the lab which is taken as  $g_{\text{lit}} = 9.811 \text{ m s}^{-1}$ <sup>1</sup>. The measured curve can be seen in fig. 2.5 and leads to the magnification factor of:

$$\text{mag} = \frac{g_{\text{lit}}}{g_{\text{fit}}} = 1.80 \pm 0.02 \frac{\mu\text{m}}{\text{Pixel}} \quad (2.19)$$

where the given error only considers the fitting uncertainty.

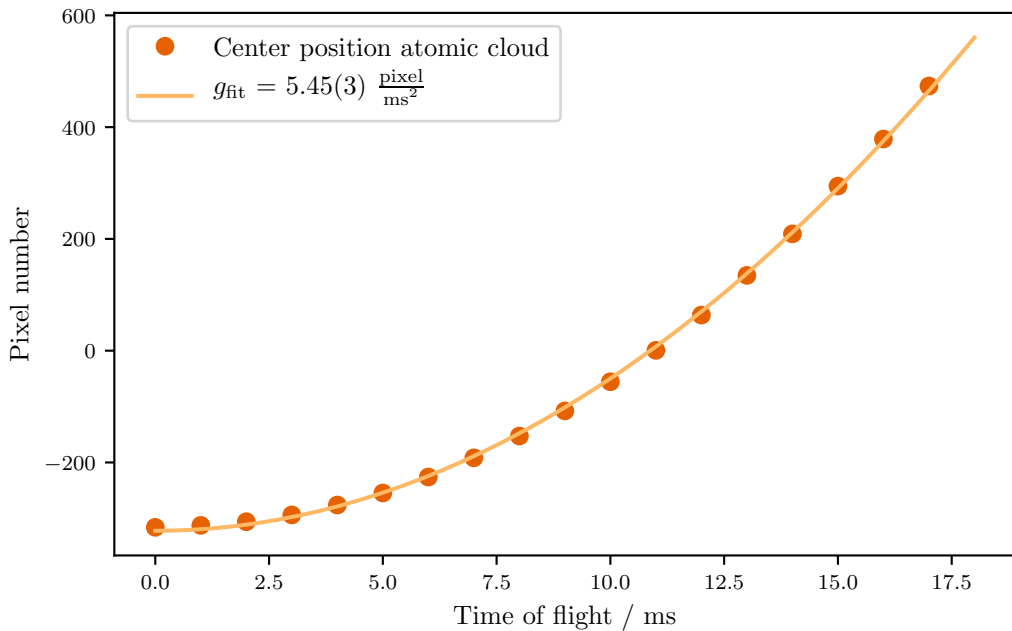


Figure 2.5: Position of the atomic cloud plotted against different TOF duration. Only one measurement per data point taken, therefore no variance for data points available.

<sup>1</sup> This estimation of the g considers its dependence on the latitude (Bonn:  $50^\circ 75'$  [47]) by using the ellipsoidal gravity formula [48].

### 2.3.8 Verification of the condensate state

Due to replacements on the experimental apparatus a readjustment of several optic paths had to be performed. Since the condensate is necessary for the following measurements with the optical lattice, a verification of the successful restoration of the condensate state is done. First indication is the observation of a transition between a classical Maxwell-Boltzmann, over a bimodal, to a Gaussian distribution of the atomic density for decreasing evaporation end powers [25]<sup>2</sup>. This passage is successfully observed and followed by a measurement of the expected aspect ratio inversion (radius inversion) in longitudinal and radial direction of the condensate during free expansion [5]. As stated in [37], this inversion is in equal shares due to repulsive inner interaction arising from the van-der-Waals interaction and non isotropic dipole-dipole interactions.

Therefore the assumed BEC with about 35 000 atoms at an end-evaporation power of 0.45 % is released from the trap and observed for TOF times between zero and twelve milliseconds. The results are plotted in fig. 2.6 and the inversion between longitudinal and radial radius is clearly observable after 6 ms, where the radii become equal.

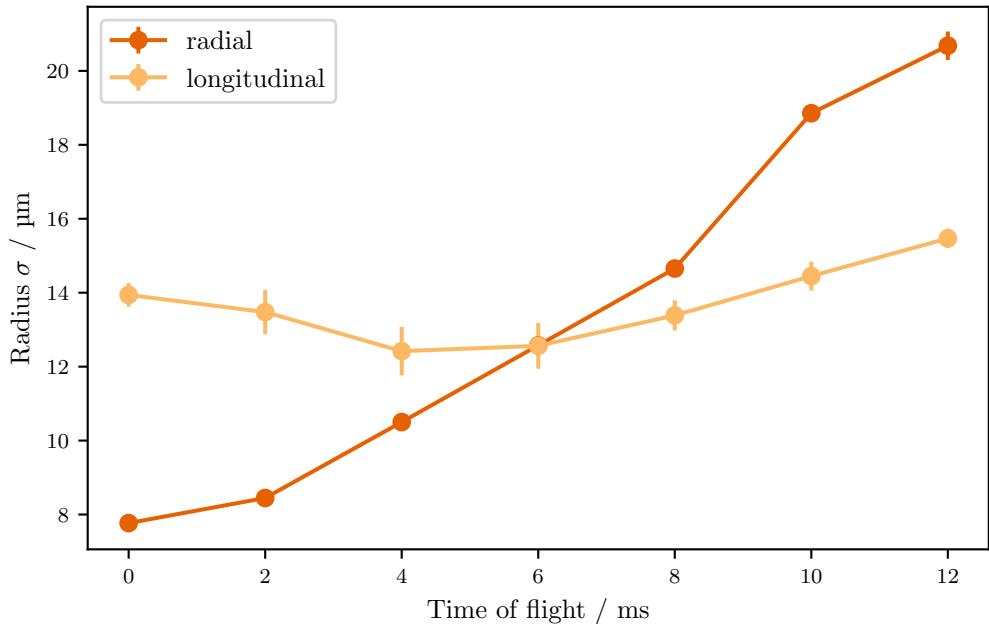


Figure 2.6: Demonstration of the aspect ratio inversion as a verification for the condensate state. Longitudinal and radial direction refer to the initial direction of the dipole trap. Three measurements for each TOF.

<sup>2</sup> It is considerable, that the precise shape of the condensate depends on the shape of the trap potential, and is not necessarily purely Gaussian.

# CHAPTER 3

---

## Characterization of the 841 nm wavelength atomic erbium transition

---

In course of the future objective to generate synthetic magnetic fields in an ultracold atomic erbium cloud there is the need for a suitable transition driving the required Raman transitions. Erbium with its complex energy structure offers several candidates. As discussed in [21] the inner shell transition with an upper state electron configuration of  $4f^{11}(^4I_{15/2}^0)5d_{5/2}6s^2(15/2, 5/2)_7^0$  and  $J = 6 \rightarrow J' = 7$  at a wavelength near  $\lambda = 841$  nm has been found to be most suitable.

So far this transition has been rarely used in Erbium experiments. However a corresponding spectroscopy and a determination of the isotope shifts have been performed already in 1990 and 1993 [49, 50]. In search of potential laser cooling transition for Erbium the group of McClelland have measured the exited state lifetime to be  $(20 \pm 4)$   $\mu$ s [36].

For Bragg scattering and the planed Raman transitions it is necessary to detune the laser by a particular frequency in the order of some Gigahertz from the mentioned transition (see chapter 4). In order to have a proper reference to frequency lock the inducing laser to a known detuning, a spectroscopy has been implemented at the atomic Erbium beam. This also allows for a confirmation of the isotope shifts.

### 3.1 Theory of optical spectroscopy

Resulting from a discrete inner energy structure, each atom and molecule offers a very unique characteristic fingerprint. When interacting with, or emitting electromagnetic radiation via absorption, spontaneous or stimulated emission, this fingerprint is measurable as a spectrum and thus making optical spectroscopy an useful tool to characterize matter. Despite the discrete nature of transmissions between different energy levels every discrete spectra and thus also the spectrum planed to observe in Erbium, is never purely monochromatic but has a spectral distribution called line profile instead [51]. This profile can be broadened by several effects, which are briefly introduced in the following.

#### Natural linewidth

Resulting from the finite lifetime  $\tau$  of an exited state, Heisenberg energy uncertainty relation  $\Delta E \cdot \tau = \hbar$  demands a unpredictability in the characteristic energy  $\Delta E$  between the exited and ground state

$\Delta E = E_e - E_g = h\Delta\nu_{eg}$  of a transition and thus leading to a natural linewidth of

$$\Delta\nu_{\text{nat}} = \frac{\Delta E}{h} = \frac{1}{2\pi\tau} \quad (3.1)$$

By approximating the excited state in the Lorentz oscillator model with the radiative energy loss acting as damping, the natural line profile can be expressed as

$$I_L(\omega - \omega_0, \gamma) = I_0 \frac{\gamma/4\pi}{(\omega - \omega_0)^2 + (\gamma/4\pi)^2} \quad (3.2)$$

with a peak intensity of  $I(\omega_0) = I_0$  and  $\omega_0$  being the transition frequency. This Lorentzian shaped function has a full width at half maximum (FWHM) of  $\Delta\omega = 2\pi\Delta\nu = \gamma$  (divided by a factor of two for the case that only radiative decay is possible). The life time is connected to the spontaneous decay rate (or sometimes: transversal relaxation rate) via  $\Delta\nu_{\text{nat}} = \gamma/2\pi = 1/2\pi\tau$ .

### Saturation broadening

If the intensity  $I$  of the excitation laser field becomes larger than the saturation intensity  $I_{\text{sat}}$

$$I_{\text{sat}} = \frac{\pi hc\gamma}{3\lambda^3} \quad (3.3)$$

of the transition, a Lorentzian shape is kept and the profile is broadened since the absorption coefficient depends on the intensity as well and becomes smaller around  $\omega_0$  for high intensities. The power broadened FWHM can be described as

$$\Delta\omega_{\text{sat}} = \Delta\omega\sqrt{1+s} \quad (3.4)$$

with  $s$  being the saturation parameter  $s = I/I_{\text{sat}}$ .

### Doppler broadening

If the observed atoms follow a velocity distribution relative to the inertial system of the observer (fluorescence) or to the of the excitation laser beam (absorption) their profile gets broadened resulting from the blue shift when moving toward the system or red shift when moving away from it. In a gas the velocities can be related to its temperature using the Maxwell-Boltzmann law, where the most probable velocity is given by:

$$v = \sqrt{2k_B T/m} \quad . \quad (3.5)$$

Here  $k_B$  is the Boltzmann constant,  $T$  the temperature and  $m$  the mass of a single particle. By integrating over the different velocity components and assuming that the decay rate  $\gamma$  is much smaller than the Doppler shift, the line shape gets dominated by a Gaussian profile

$$I_G(\omega, \Delta\omega_D) = I_0 \exp\left(-\left(\frac{\omega - \omega_0}{\sigma}\right)^2\right) \quad (3.6)$$

with the associated Doppler width:

$$\Delta\omega_D = \omega_0 \sqrt{\frac{8k_B T \ln(2)}{mc^2}} \quad (3.7)$$

that relates to  $\sigma$  as

$$\sigma = \frac{\Delta\omega_D}{2\sqrt{2 \ln(2)}} \quad . \quad (3.8)$$

When considering an atomic beam instead of a thermal cloud, it is important to notice that the transversal velocity  $v_x$  is lower than mean velocity of the atoms in a gas with temperature  $T$ . Depending on the quality of collimation the Doppler width needs to be reduced by a factor of  $C$

$$\Delta\omega_{x,D} = \Delta\omega_D \cdot C \quad (3.9)$$

Where  $C = v_x/v$  can be taken as an indicator for the beam collimation and is directly correlated to the opening angle of the beam  $\epsilon = \arcsin C$  (for a more detailed description please refer to Ch. 9.1 [52]).

In some systems where the gas is under high pressure and temperature, the particle interaction happens with much higher rates and collision broadening can play a significant role. Since in this experiment the atomic gas is very dilute this effect is considered negligible.

If saturation and Doppler broadening act at the same time and with comparable influence, the resulting line profile needs to be treated by a convolution of the Lorentzian and Gaussian shaped distributions which is represented by a Voigt profile:

$$I_V(\omega, \Delta\omega_{x,D}, \Delta\omega_{\text{nat}}) = \int_{-\infty}^{+\infty} I_G(\omega', \Delta\omega_{x,D}) \cdot I_L(\omega - \omega', \Delta\omega_{\text{nat}}) \, d\omega' \quad (3.10)$$

With an approximation for the total linewidth of [53]:

$$\Delta\omega_V \approx 0.5346 \cdot \Delta\omega_{\text{sat}} + \sqrt{0.2166 \cdot \Delta\omega_{\text{sat}}^2 + \Delta\omega_{x,D}^2} \quad (3.11)$$

## 3.2 Set-up of the atomic beam spectroscopy

Due to its long lifetime and thus very narrow natural linewidth of 8 kHz an absorption spectroscopy of the 841 nm transition is not as straightforward as for the already implemented 401 nm transition which offers an approximately 4400 times larger linewidth. This paired with the Titan:Saphir-Laser (Ti:Sa) laser source which supplies a linewidth no better than 100 kHz results in several broadening effects which make it hard to resolve an amplitude with good contrast in the probe beam. Observing a fluorescence signal in contrast has the advantage of measuring from theoretically zero amplitude and thus use sensitive detection tools like a photo-multiplier or an avalanche photodiode.

The challenge of this set-up is to implement a spectroscopy at the already existing transversal cooling (TC) view ports without disturbing the cooling set-up and thus interfere with the functionality of the whole experiment. The 841 nm light is transported to the TC with an optical fiber. Coming from the out-coupler (*Schäfter & Kirchhoff: 60FC-4-M8-10*) it is overlayed with the ellipsoid shaped 401 nm transversal cooling beam using a D-shaped mirror. As shown in fig. 3.1 the beam is directed through

the atom beam perpendicular to its propagation axis with a beam diameter of about  $(2.0 \pm 0.3)$  mm. On a platform above the TC the excitation beam gets dumped on one side and a lens with focal length of 100 mm collects the fluorescence light from the other direction and guides it onto a photomultiplier tube (PMT) (*Hamamatsu R928 with C6270*). The PMT is protected from thermal radiation coming from the oven via a band pass filter centered at  $(840 \pm 2)$  nm and  $FWHM = 10$  nm (*ThorLabs: FB840-10*). The detection set-up is carefully aligned using the 401 nm light on the same outcoupler and thus the same beam path. The much stronger fluorescence of this transition which is in the visible range can be captured with a camera for coarse alignment of lens and mirror. Observing the PMT signal, adjustments at the lens distance and reflecting mirrors are done until the best signal is archived. Limited by the existing shielding and mounting structure (as illustrated in fig. 3.3) the lens with an effective collection area of  $r = 2.54$  cm (two inch) could only be placed at a distance of approximately  $R = (46.6 \pm 4.0)$  cm from the excitation region. Since the fluorescence is radiated isotropic in all  $4\pi$  the set-up can only receive light from a solid angle of approximately  $\Omega = 2\pi r/R^2 = 18.7$  msr, which corresponds to a fraction of about 0.15 % of the total emitted fluorescence.

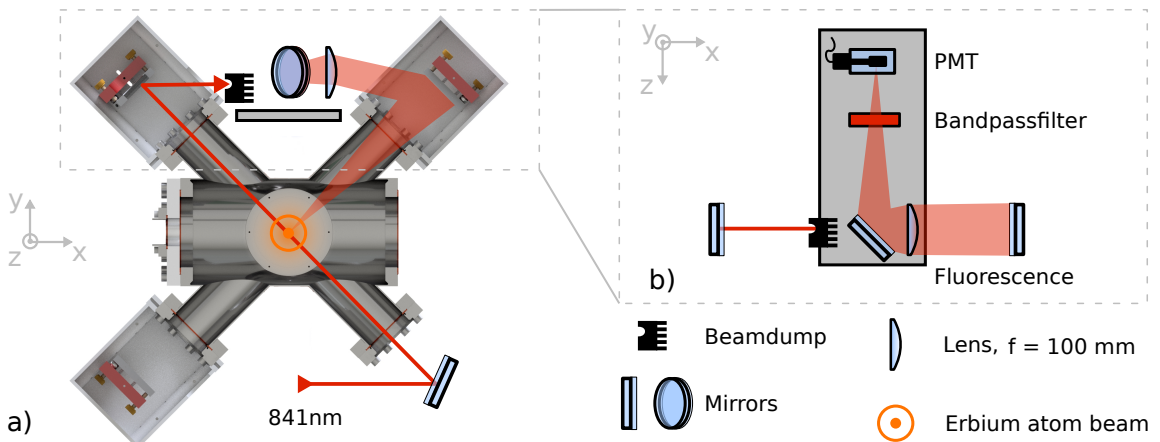


Figure 3.1: Optical spectroscopy set-up at TC a) Cross section through TC and atomic beam. Atom moves towards the observer. b) Top view of the TC. All optics have two inches diameter. Sketch not to scale. See fig. 3.3 for a picture of the set-up.

The PMT signal is fed to a lock-in amplifier (*Signal Recovery model 7265*), which is set to a  $10\mu\text{s}$  time-constant and  $100\mu\text{V}$  sensitivity. The excitation beam is chopped at 1 kHz using an acousto-optic modulator (AOM). Since a large portion of the noise seems to come from the scattered light of the laser itself, the best spectroscopy signal is obtained averaging over 64 scan cycles which then leads to the spectrum displayed in fig. 3.2.

The spectrum is obtained with the Ti:Sa being externally scanned by a sawtooth function of 0.155 Hz over a total scan range of  $(4.20 \pm 0.08)$  GHz (scanspeed  $1.3\text{ GHz s}^{-1}$ ). In this case the absolute scan range is quantified with a wavemeter (*HighFinesse WS-6*, relative resolution  $\pm 0.0001$  nm), which results in a large error that rescales the x-axis in total and makes a quantifiable evaluation not sensible. At this point an appropriate Fabry-Pérot resonator is a better choice to reduce this error. Yet, the absolute isotope distance is not of main interest for the purpose of the over all experiment and such can be overlooked. The excitation beam has a power of  $P = (46 \pm 2)$  mW which corresponds to an intensity of  $(730 \pm 220)$  mW  $\text{cm}^{-2}$  which is five magnitudes larger than the saturation intensity.

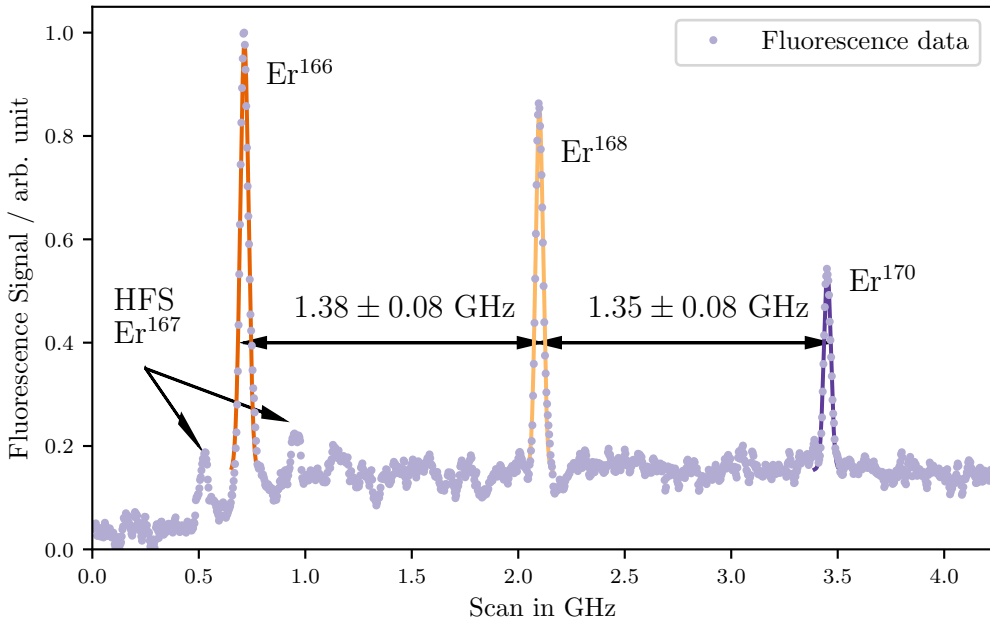


Figure 3.2: Fluorescence signal near 841 nm, averaged over 64 scan cycles measured with a PMT on the erbium atomic beam at the TC stage. In order to determine the isotope shifts, Gaussian fits are applied. The thereby measured distance between their mean values is noted within the graph. Arrows mark the two noticeable hyperfine structure (HFS) peaks of  $\text{Er}^{167}$  and the isotope shift.

As discussed in section 3.1, the broadened natural line width can be calculated as 5.20 MHz. Comparing this value with the FWHM of one fitted Gauss peak  $\text{Er}_{\text{FWHM}}^{168} = 41 \text{ MHz}$  shows that the measured width is one magnitude larger in experimental observation. This can be explained by the fact, that the beam of erbium atoms can not be assumed to be sufficiently collimated when coming from the apertures and thus has velocity components traveling not only perpendicular to the excitation beam leading to a Doppler-broadening effect. Furthermore is it assumed, that the frequency of the scanned laser might drift slightly during the measurement time of about four minutes and thus the averaging process not only reduces the noise but also broadens the width.

Clearly visible are the three isotopes  $\text{Er}^{166}$ ,  $\text{Er}^{168}$  and  $\text{Er}^{170}$  showing their descendant abundance with higher wavelength as well as at least two of the hyperfine structure peaks of  $\text{Er}^{167}$ . Despite the described precision issues we can extract the isotope distance to be:

Isotopes	Measured	Literature Value [49]
166 - 168	$(1.38 \pm 0.08) \text{ GHz}$	$(1.433 \pm 0.001) \text{ GHz}$
168 - 170	$(1.35 \pm 0.08) \text{ GHz}$	$(1.476 \pm 0.002) \text{ GHz}$

Which, considering the large uncertainty, is in accordance to the literature values. Possible improvements to the current set-up could be an enlargement of the excitation beam diameter, since more power is available this could result in a slightly higher fluorescence signal. Even better would be to reconstruct the metal shielding around the TC and move the lens closer to the chamber

window to increase the solid angle. If the measurement rate, which for now is limited by the PMT signal, would be increased without loosing sensitivity, it could be possible to perform a lifetime measurement on the atom beam.

With the current status is now possible to define a common detuning  $\Delta$  of the Bragg/Raman beam near to the  $\text{Er}^{168}$  line with a precision primary limited by the used wavemeter. Since the planed detuning is to large for common frequency shifting tools like AOM or electro-optic modulator (EOM), possible options for a more precise laser locking scheme could be:

- The laser could be locked to the  $\text{Er}^{166}$  isotope line using the Pound–Drever–Hall technique. This option has the disadvantage of being limited to one fixed detuning but on the other hand is relatively simple to install with a sufficiently high and stable spectroscopy signal. [54]
- Using an external cavity with ultra low expansion characteristics enables free choice of the detuning and offers a reduction of the laser bandwidth, limited by its internal control technique.

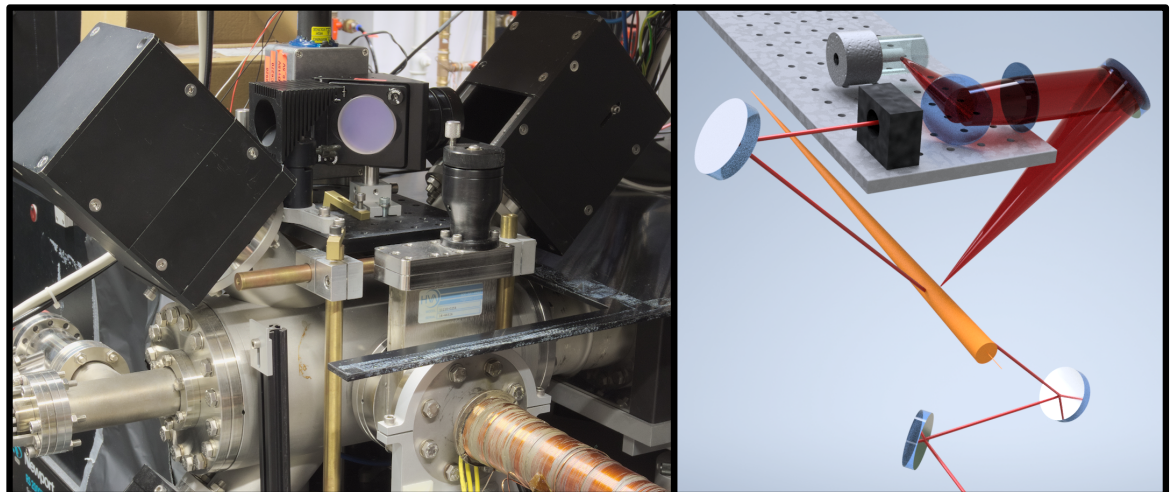


Figure 3.3: Transversal cooling stage including the new spectroscopy set-up. Left: Picture of the set-up in place. Right: Rendered image of the set-up. The atomic beam coming from the oven is illustrated in orange. The diverging red light represents the fraction of the emitted 841 nm fluorescence which can be collected from the set-up.

## CHAPTER 4

---

# Diffraction of cold erbium atoms off a one-dimensional standing wave

---

Optical lattices are commonly formed by using interfering laser beams resulting in a periodic standing wave potential which interacts with an atomic ensemble. That such a lattice potential could act as a grating to diffract neutral atoms was first suggested in 1966 [55, 56] and successfully carried out by D. Pritchard and his coworkers using a beam of Sodium atoms in 1983 [57, 58]. The first diffraction of atoms from a BEC was achieved by the group of W. D. Phillips in 1999 [59].

Continuing this idea, V.S. Letokhov proposed in 1968 that not only diffraction but also the confinement of ultracold atoms in wavelength size regions of standing light waves should be possible [60]. Since then, the field has rapidly developed, going from one dimension to the confinement of ultracold atoms in two or three dimensional structures [40].

The great interest in this field arises from the possibility to simulate various quantum mechanical systems. In contrast to solid state physics, which investigates the behavior of electrons in crystal lattices, ultracold atoms in optical lattice potentials overcome the difficulty of crystal defects and open up the possibility to experimentally control the lattice properties. This bridge to condensed matter physics allows the study of several physical models, such as the Bose-Hubbard model or Mott insulator transitions [61].

The following chapter starts with an introduction to optical lattice potentials, describing the underlying theoretical concepts and necessary definitions. Then the newly implemented one-dimensional lattice potential set-up is described in detail and finally the first measurements of a diffracted ultra cold Erbium ensemble using radiation tuned near a narrow-line transition are presented and discussed.

### 4.1 Optical lattice

As for the optical dipole trap, the underlying principle for the optical lattice potential arises from the ac Stark shift, just that in the case of an one dimensional lattice potential the oscillating electric field is created by two interfering laser beams where the resulting standing wave modulates the energy levels periodically. The two beams ( $i = 1, 2$ ) can generally be described by plane waves with polarization axis  $\vec{e}_i$ , frequency  $\omega = 2\pi\nu$ , wave vector  $\vec{k}$  and phase  $\phi_i$  [62]:

$$\vec{E}_i(\vec{r}, t) = \vec{e}_i E_i \cos(\omega_i t - \vec{k}_i \cdot \vec{r} + \phi_i) \quad (4.1)$$

For the case of counter-propagating waves along the z-axis as illustrated in fig. 4.1 with parallel linear polarization<sup>1</sup>, same wavelength  $\lambda$  ( $\omega_1 = \omega_2$ ) and a constant phase this simplifies to:

$$\vec{E}_1(z, t) = \hat{\vec{e}}_1 E_1 \cos(\omega t - kz) = \hat{\vec{e}}_1 E_1 \left[ e^{i(\omega t - kz)} + e^{-i(\omega t - kz)} \right] \quad (4.2)$$

$$\vec{E}_2(z, t) = \hat{\vec{e}}_2 E_2 \cos(\omega t + kz) = \hat{\vec{e}}_2 E_2 \left[ e^{i(\omega t + kz)} + e^{-i(\omega t + kz)} \right] \quad (4.3)$$

Where  $k = |\vec{k}| = 2\pi/\lambda$  can be considered as the corresponding wavenumber. The intensity of the resulting light field is defined over the time average as

$$I(z) = c\epsilon_0 \langle \vec{E}(z, t)^2 \rangle_t \quad (4.4)$$

$$= c\epsilon_0 \langle (\vec{E}_1 + \vec{E}_2)^2 \rangle_t \quad (4.5)$$

$$= c\epsilon_0 \langle \vec{E}_1^2 + \vec{E}_2^2 + 2\vec{E}_1 \cdot \vec{E}_2 \rangle_t \quad (4.6)$$

$$= I_1 + I_2 + I_{\text{int}}(z) \quad (4.7)$$

and in the end consists of two spatial independent intensities  $I_1$  and  $I_2$  and an interference term  $I_{\text{int}}(z)$  that depends on the position along  $z$  and is calculated from eqs. (4.2) and (4.3) as<sup>2</sup>

$$I_{\text{int}}(z) = 2\sqrt{I_1 I_2} \cos(2kz) \quad (4.8)$$

As for the dipole trap, the red detuning to a corresponding atomic transition of both beams leads to a field gradient that results in an attractive force towards the intensity maxima and the spatial dependent optical lattice potential follows as:

$$V_L(z) = \frac{V_0}{2} \cos(2\pi z/d) \quad (4.9)$$

with the lattice spacing  $d = \pi/k = \lambda/2$  and the lattice depth  $V_0 \propto \sqrt{I_1 I_2}$ . For a optical lattice with beams of same polarization and intensity, the height of the barrier between minima and maxima reduces to  $V_0 \propto \frac{\hbar\Omega_R^2}{\Delta}$  where  $\Omega_R$  represents the Rabi frequency and  $\Delta$  the detuning to the transition [24].

Resulting from these calculations it is common to describe the optical lattice properties using some characteristic parameters [61]. The mentioned lattice depth  $V_L$  is typically given in units of the

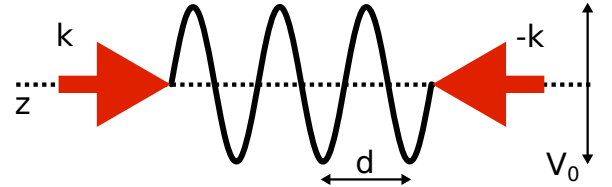


Figure 4.1: Atomic standing wave potential trealized with two counter propagating beams. With lattice spacing  $d$  and lattice depth  $V_0$

<sup>1</sup> For two beams which impinge under an angle  $\theta$  the scalar product of the two wave vectors must be treated as  $\vec{r}(\vec{k}_1 + \vec{k}_2) = k \cdot z \cdot \cos(\theta/2)$  instead.

<sup>2</sup> For parallel polarization the interference becomes maximal. With an angle  $\alpha$  between the orientation of the two linear polarization axes the scalar product has to be treated as  $\hat{\vec{e}}_1 \cdot \hat{\vec{e}}_2 = \cos(\alpha)$ . In addition a phase difference  $\phi = \phi_1 + \phi_2$  allows for the shift of the spatial position of the lattice potential and the final interference term becomes  $I_{\text{int}}(z) = 2\sqrt{I_1 I_2} \cos(2kz + \phi) \cdot \cos(\alpha)$

recoil energy  $E_R$  which is defined by the energy a photon with the momentum

$$p_\gamma = \hbar k \quad (4.10)$$

transfers to an atom with mass  $m$  in an absorptive processes:

$$E_R = \frac{p_\gamma^2}{2m} = \frac{\hbar^2 k^2}{2m} = \frac{\hbar^2 \pi^2}{2md^2} \quad . \quad (4.11)$$

From this the dimensionless parameter  $s_L = V_0/E_R$  and the recoil frequency  $\omega_R = \frac{E_R}{\hbar} = \frac{2\hbar\pi^2}{m\lambda^2}$  are deduced<sup>3</sup>. Considering the wavelength of the used lattice beams as well as the mass of the Er<sup>168</sup> isotope it is possible to calculate the key parameters for the implemented lattice potential to be:

$\lambda$	$d$	$p_\gamma$	$E_R$	$\omega_r$
841 nm	421 nm	$7.87 \times 10^{-28} \text{ kg m s}^{-1}$	$1.11 \times 10^{-30} \text{ J}$	10.52 kHz

Table 4.1: Characteristic values for the implemented lattice with 840.990 nm.

As the periodic potentials can be compared to an arrangement of spaced dipole traps, it is possible to assign a harmonic oscillation frequency which describes the lattice oscillator period  $t_L$  of the atoms within one of those wells as

$$\omega_L = \frac{\pi}{d} \sqrt{\frac{2V_0}{m}} = \frac{2\pi}{t_L} \quad . \quad (4.12)$$

Depending on the magnitude of  $V_0$ , it is common to differentiate between two limits. In the case of the *shallow-lattice* (or *weak potential*) limit which holds for  $s_L \approx 1$ , the wavefunction of an atom localized at a designated lattice site, is overlapping with other lattice sites, giving rise to interesting effects as Bloch oscillations and Landau-Zener transitions. For the *deep lattice* (or *deep periodic potentials*) limit with  $s_L \gg 1$ , the wave functions are localized and tunneling between the different lattice sites is strongly suppressed [61][IV. A]. Since this experiment focuses on the deep limit, it is reasonable to waive on a deeper explanation of any tunneling effects in the following.

### 4.1.1 Diffraction on an optical lattice

In analogy to classical optics where a coherent beam of light which gets diffracted by a grating results in a characteristic diffraction pattern, in atom optics the optical lattice can serve as a grating for the atomic matter waves which is realized by a BEC.

Following [24] and [37], the Schrödinger equation for a single particle moving in the periodic potential with the corresponding Hamiltonian  $\hat{H}$  including the optical lattice potential  $V_L$  takes the following form:

<sup>3</sup> In this work the recoil energy refers to the momentum a single photon carries. In the literature the definitions sometimes vary by a factor of 4 due to the actual two photon process. A process with  $n$  photons  $p_{n\gamma} = n \cdot p_\gamma$  and  $E_{R,n\gamma} = n^2 \cdot E_R$  shall be defined as notation here.

$$i\hbar \frac{\partial}{\partial t} \Psi = \hat{H}\Psi = E\Psi \quad (4.13)$$

$$\hat{H} = -\frac{\hat{p}^2}{2m} + V_L(z) \quad (4.14)$$

$$= -\frac{\hbar^2}{2m} \frac{d^2}{dz^2} + V_L(z) \quad (4.15)$$

where  $E$  is the energy for a certain state. Under the assumption that the atoms are only moving along the  $z$ -direction, the Hamiltonian is reduced to one dimension. In general it is not possible to solve this Schrödinger eq. (4.13) in an analytic way.

Therefore an attempt can be made to tread the process in different regimes. For lattice interaction times  $\tau$  in the order of  $\tau \ll t_L \lesssim \frac{1}{\omega_r}$  it is sufficient to describe the effect in the so called *Raman-Nath regime*, which is in close analogy to the diffraction on a thin grating in classical optics [63], [61]. For larger interaction times, on the other hand, we consider the *Bragg regime* which can be compared to a thick grating in classical optics. The mathematical ansatz to this regime is done by only considering a finite number of diffracted orders which couple to another and reduce the problem to a system similar to the well known problem of a two-level Rabi system.

### Bragg regime

The  $n$ -th order Bragg diffraction can also be understood as  $2n$ -photon stimulated Raman process [59]. As illustrated in fig. 4.2(b) for a moving lattice which is characterized by a detuning of  $\delta$  between the two lattice beams, the atom absorbs a photon from one of the beams and reemits another photon into that beam via stimulated emission. It is important to notice that this process happens instantaneous and due to the larger detuning  $\Delta$  the atom shall not be considered to be in the exited state at any time. Considering the electric field composed of the two laser beams, energy conservation leads to a change of the external state of the atom. The internal state of the atom does not change during or after the process and remains in the ground state. The Bragg condition for this process reads as:

$$\frac{(n \cdot 2 \cdot p_\gamma)^2}{2m} = n\hbar\delta_n \quad . \quad (4.16)$$

By experimentally adjusting the detuning  $\delta$  between these two beams it is possible to fulfill the Bragg condition and observe diffraction of  $n$ -order with

$$\delta_n = n \cdot \delta_1 = n \cdot 42 \text{ kHz} \quad . \quad (4.17)$$

### Raman-Nath regime

Following the explanation by W. D. Phillips [63] and P. Meystre [58] the kinetic term in the Hamiltonian is neglectable for short interaction times, because the transverse kinetic energy of the atoms can then be assumed to be small compared to the interaction energy and the atomic velocity can be ignored. In

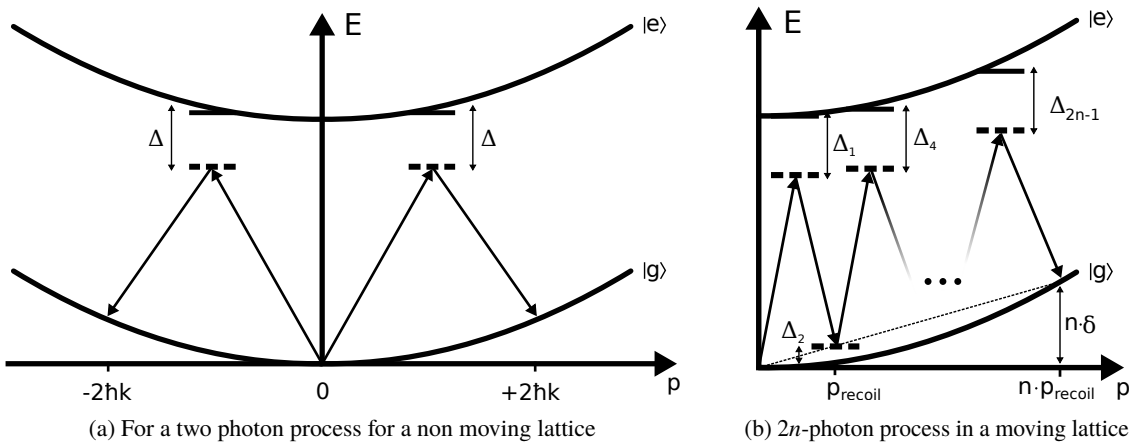


Figure 4.2: Illustration of the stimulated Raman process in an energy momentum graph.

this case the BEC splits into multiple components with momenta

$$p_n = n2\hbar k \quad (4.18)$$

where the relative population in every order oscillates, depending on the pulse duration. A beautifully illustration of the resulting pattern is shown by I.B. Spielman, W.D. Phillips and colleagues [64]. By solving the Schrödinger equation with the mentioned approximation<sup>4</sup> it is possible to estimate the probability for atoms to be in a transverse momentum state  $n$  after the pulse time  $\tau$

$$P_n(\tau) = J_n^2(\Omega_0\tau) \quad (4.19)$$

where  $J_n^2$  is the  $n$ -order Bessel function and  $\Omega_0$  the Rabi frequency which scales with the lattice depth and the detuning from resonance  $\Delta$  as  $\Omega_0 = V_0\Delta/\hbar$ .

A rough estimation of the lower limit of the lattice depth can already be gained by observing the highest visible diffraction order, which then corresponds to the maximal momentum transfer of  $p_{\max} = 2\hbar k_{\max} = n_{\max}2\hbar k$

$$V_0 = 4n_{\max}E_R \quad (4.20)$$

The diffraction into multiple orders can also be understood as consequence of the energy uncertainty which plays a role due to the very short interaction time with the lattice beams. When the pulse time increases, the number of observed diffraction orders is limited. The momentum transfer from the  $2n$ -photons is clearly resolvable and only  $\pm n^{\text{st}}$  diffraction orders that fulfill the Bragg condition are observable.

<sup>4</sup> See [58] section 4.1.1 for a more detailed derivation.

## 4.2 Experimental realization of an one-dimensional optical lattice potential

The optical lattice potential in this experiment is realized by using laser light from the Ti:Sa source supplying a maximum of about 3 W at 841 nm in total. As shown in fig. 4.3 the Ti:Sa light is split up using a polarizing beamsplitter (PBS) and a  $\lambda/2$ -waveplate with which the power distribution among the paths can be adjusted. One of the paths is used for additional probing purposes, such as the spectroscopy described in chapter 3, the wavemeter or a Fabry-Pérot interferometer to check the stability during frequency scans. The other path is again split up and used for the two lattice beams (due to their future use as beams for Raman manipulation they will be labeled as R1 and R2).

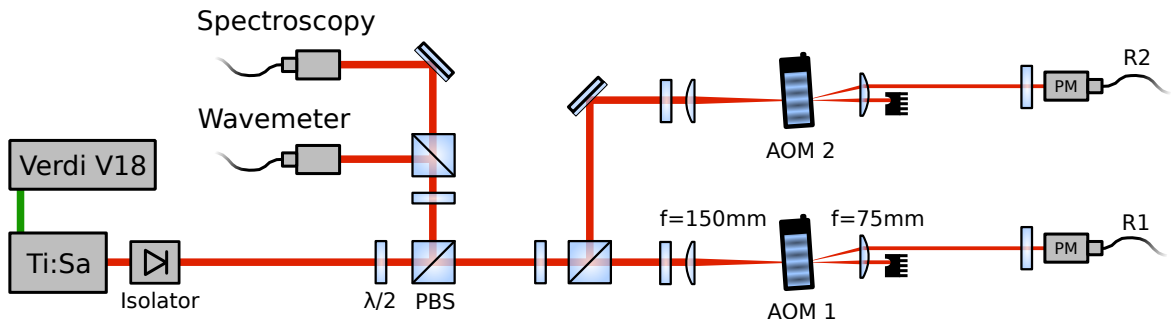


Figure 4.3: Optical set-up for the preparation of the two lattice beams.

Each of the beams passes a  $\lambda/2$ -waveplate in order to align the polarization axis of the beam to that of the AOM crystal. Coming from the laser with a beam radius of  $w = (0.55 \pm 0.06)$  mm<sup>5</sup> it gets focused using a focal length of  $f = 150$  mm, resulting in a theoretical minimal beam waist of  $w_{\min} \approx \lambda \cdot f / \pi \cdot w_0 \approx 0.073$  mm [65]. The beam size is correlated to a trade-off between higher diffraction efficiency for larger diameters and faster switching times for smaller diameters. With the AOM mounted on a translation stage it can be moved along the laser focus and an experimental optimum is found at a measured radius of approximately  $w = (0.23 \pm 0.10)$  mm. A larger uncertainty on this value results from the imprecise positioning of the knife-edge at the initial position of the AOM crystal. The measured diffraction efficiency was measured to be 83 %. Only the first diffracted order is used and recollimated using a 75 mm focal length lens to gain the necessary beam size for coupling into the fiber (optimum:  $w = 0.5$  mm). Since constant polarization and power is necessary for the planned experiments, a polarizing maintaining fiber is installed.<sup>6</sup> In order to match the fast axis of its PANDA structure with the linear polarized light, a  $\lambda/2$ -waveplate is installed in front of the fiber coupler [66]. A  $\lambda/2$ -plate with a rotating Wollaston Prism might be considered as alternative adjustment to compensate for non purely linear polarized light which would result in fluctuations at the end of the fiber. Best measured transmission efficiency through the fiber was 50 %.

### Radio frequency set-up

To drive the acousto-optic modulators, different radio frequency (RF)-components are assembled as illustrated in fig. 4.4. As signal source a two-channel arbitrary function generator is chosen to

<sup>5</sup> In this work the beam radius  $w$  is always referred to as being the  $1/e^2$  width, corresponding to a  $FWHM = w \cdot \sqrt{2 \ln 2}$ .

<sup>6</sup> Coupler: 60-FC-4-M5-10, Fiber: PMC-E-780-5.1-NA012-3-APC-EC-1000-P, Collimator: 60-FC-4-A8-07

ensure that both output signals are in-phase with each other. The generator is connected via local area network (LAN) to the computer, running the experiment software. A new control phase is implemented, where parameters for on/off-state, amplitudes and frequencies can be set. For every new experimental cycle the function generator is updated with the chosen parameters. Since the center frequency of the used AOM is at 200 MHz but the maximum output frequency of the generator is at 100 MHz a RF-frequency doubler is used to transfer to the proper range. The following high- and low-pass filter are intended to damp other orders of the multiplied signal.

To perform measurements of Rabi oscillation in the Raman-Nath regime, a minimal pulse duration of about one microsecond, placed at a precise moment during the whole experimental sequence, is expected to be necessary. Therefore a RF-switch is used which gets triggered with a TTL-signal coming from the real time *ADwin*-system. The experiment software is extended further, to address the real time system and allow the choice for different number of induced pulses and their duration over the graphical user interface.

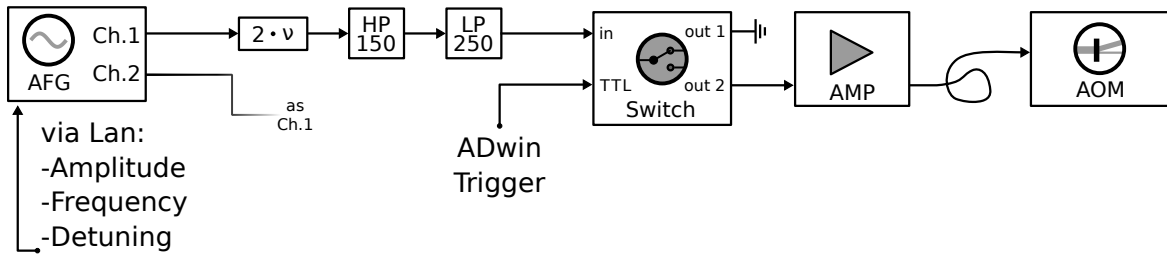


Figure 4.4: RF electronics setup for the creation of Bragg pulses with an AOM. Legend (from left to right): Tektronik arbitrary function generator AFG3102C, MiniCircuit: Frequency multiplier FD-2+, highpass filter BHP-150, lowpass filter BLP-250, switch ZYSWA-2-50DR+, amplifier ZX60-8008E+ and ZHL-1-2W+, Gooch&Housego AOM 3200-124.

### Aligning the lattice beams

The optical fibers transport both beams to the main chamber of the experiment. Due to the limited number of free viewports and because of the configuration of already existing magnetic coils which are intended to be used in the future, the lattice axes is chosen to be overlaid with one of the MOT axis as illustrated in fig. 4.5. To achieve a defined polarization both beams get reflected by a PBS after exiting the collimator. Using dichroic mirrors they are overlaid with the 583 nm beams of the MOT.

To align the lattice beams, fiber R1 gets replaced with a probe beam of resonant 583 nm and an atomic cloud is captured in the MOT. In a next step the atoms are confined in the dipole trap, which is much smaller than the rather large MOT cloud and a pulse of resonant light is shot into the chamber just before an absorption image is taken. By spatially scanning the beam in small steps and for each step observing a new absorption image it is possible to find an intersect with the dipole trap since in that case the probe beam eliminates atoms in the trap which is visible as a hole in the absorption image. After this, the beam R2 is overlayed with the probe beam using the long common beam path. In a final step we interchange the fiber on collimator R2 and in an iterative way adjust the beam path such that the light from R1 gets coupled into fiber R2 and vice versa.

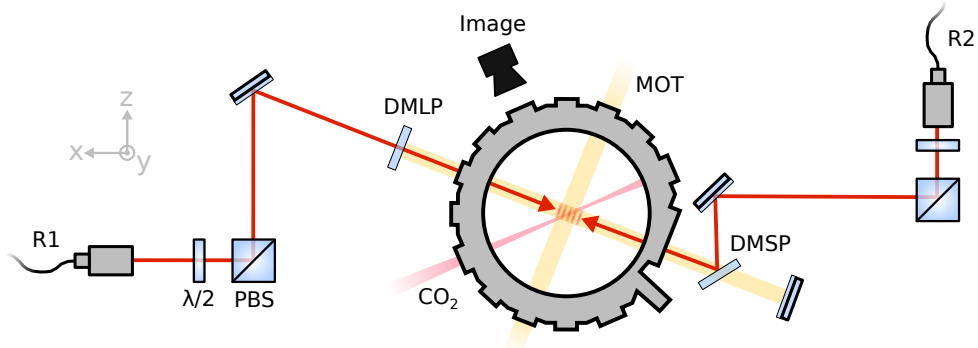


Figure 4.5: Optical set-up for the lattice beams at the vacuum chamber using dichroic longpass (DMLP) and shortpass (DMSP) mirrors for overlaying the 841 nm lattice beams with one axis of the 583 nm MOT beams. The illustrated CO<sub>2</sub>-laser dipole trap as well as the absorption image system are oriented in an angle of 45° to the lattice beams, respectively.

### Characterization: Beam waist at atomic cloud

As introduced in section 4.1 defining parameters for the properties of an optical lattice potential are the intensity and pulse duration which describe the lattice depth and interaction time, respectively. As the intensity for a fixed power scales with the beam size, we can approximate the intensity with a homogeneous distribution over the beam radius by

$$I = \frac{P}{A} = \frac{P}{2\pi w^2} \quad (4.21)$$

where  $A$  represents the beam area approximated over the beam waist  $w$ . For each lattice beam the radius is measured directly after the collimator and at the position of the cloud. Since it is not possible to measure within the vacuum, the beam path is reconstructed beside the chamber with distances of  $D_{R1} = (104 \pm 3)$  cm and  $D_{R2} = (150 \pm 3)$  cm between collimator and cloud. The resulting beam radii, measured using the knife-edge method as described in [67, 68], are shown in fig. 4.6.

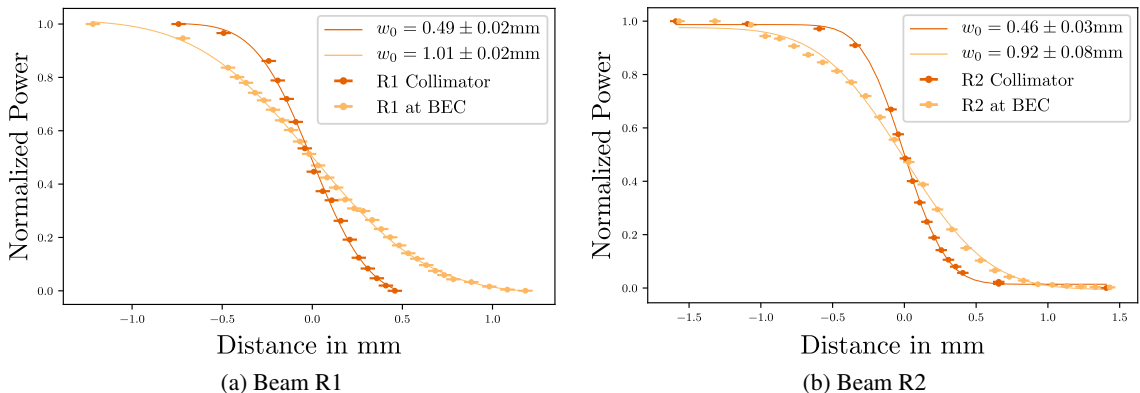


Figure 4.6: Beamwaist measured with the knife-edge method. Directly after the collimators and at the approximated position of the cloud. The here given errors on the radius represents one standard deviation of the estimated error of the fitted parameter.

Due to the rather large distances of  $D_{R1}$  and  $D_{R2}$  the beam diverges by a factor of about two in total. The beam waists at the position of the cloud is measured to be:

$$w_{1,\text{cloud}} = (1.01 \pm 0.06) \text{ mm} \quad w_{2,\text{cloud}} = (0.92 \pm 0.06) \text{ mm}$$

### Characterization: Pulses

To test if all elements within the pulse generation procedure behave as expected from their specifications and are able to fulfill the experimental requirements, a photodiode is installed in transmission direction of both PBS at the chamber (see fig. 4.5). This is also helpful during daily operation to check if the polarization or, the power in the lattice beams fluctuates on short and long timescales.

Using the experiment software, a single pulse with a duration of  $3 \mu\text{s}$  at maximum RF-power is send to the switches and the resulting light collected with the photodiodes is recorded with an oscilloscope, shown in fig. 4.7.

A small offset of about  $\Delta_{\text{start}} = (0.32 \pm 0.05) \mu\text{s}$  between the beginning of both pulses is registered,

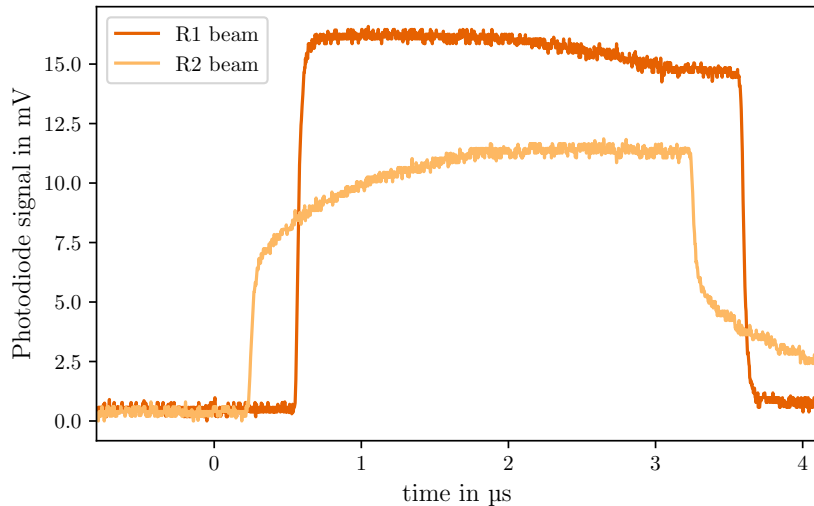


Figure 4.7: Laser pulses measured at chamber for R1 and R2.  $3 \mu\text{s}$  pulse on each channel.

even though same length for all transmission lines are chosen. Considering the acoustic velocity in the crystal, specified as  $4.2 \text{ mm } \mu\text{s}^{-1}$ , it might be concluded that the difference comes from different entry point of the foci in the crystals. As illustrated in fig. 4.8, the obtained rise times are:

$$t_{R1,\text{rise}} = 53 \text{ ns} \quad t_{R2,\text{rise}} = 878 \text{ ns} \quad .$$

The spatial broad beam radius interacting with the acoustic wave in the AOM crystal leads to a limit in rise time as stated by the specifications. For a smaller beam radius ( $20 \mu\text{m}$ ) shorter rise times are achievable (10 ns) for the used model. To prevent exceeding of the optical power density and to increase diffraction efficiency the larger diameter is chosen. Beam one shows a steep continuous rise with a rise time in the magnitude as expected. Whereas beam 2 rises to 50 % in the approximate same time but then develops a longer slope to achieve the maximum amplitude. An interchange of the RF

supply paths clarifies that the error does not originate from there. It is expected, that this effect is due to an imperfect alignment of the laser beam through the second AOM crystal. A realignment of the second AOM using a pulsed laser during alignment should overcome this problem.

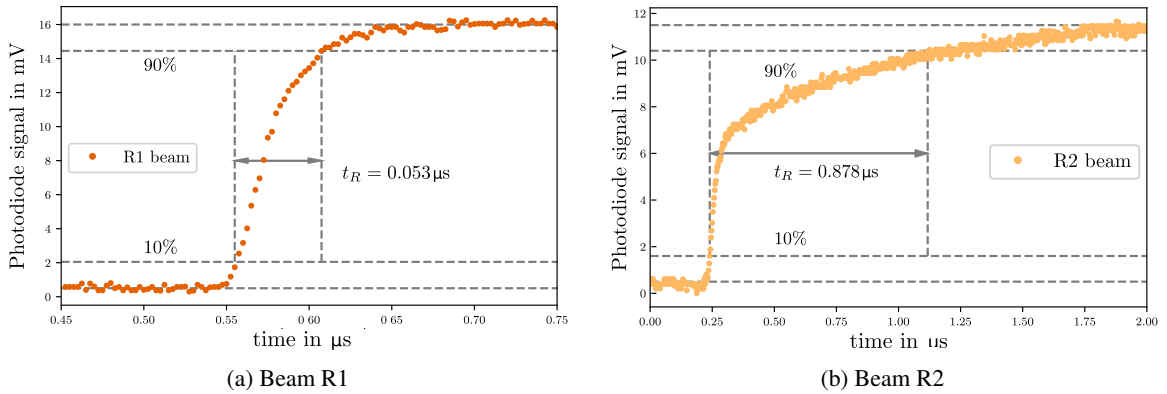


Figure 4.8: Rise time measurement behind the optical fiber. Rise time defined as time where the amplitude of the signal goes from 10 % to 90 %.

### 4.3 Observation of a diffracted atomic erbium condensate

Before using the lattice beams it is verified in a separated measurement, that the atomic cloud of erbium atoms is sufficiently cold by observing a bimodal density distribution as well as a radius inversion (see section 2.3.6) for the selected end power of the evaporative cooling process.

The BEC is suddenly released, by instantaneous switching off the  $\text{CO}_2$ -laser dipole trapping beam. To reduce potential atomic interaction arising from a very dense condensate, the atomic gas is allowed to expand for 2 ms before instantly switching on both lattice beams for an interval of  $20\mu\text{s}$ . At this point, each beam has a power of about  $(150 \pm 20)\text{ mW}$ , corresponding to a mean intensity of  $I = (2.56 \pm 0.34)\text{ W cm}^{-2}$  per beam. After the short interaction with the lattice beams the cloud(s) expand freely in the earth gravity field for a TOF of 14 ms before the atomic distribution is recorded with an absorption image. A detailed illustration of the timing sequence can be obtained from fig. 4.11(a).

With the chosen parameters it was possible to observe a splitting of condensate atoms with on average  $28\,000 \pm 2\,000$  atoms as shown in fig. 4.9. Clearly visible are the two side peaks with smaller densities and the initial BEC with most of the atom population in the middle. The measurement was reproducible multiple times and the splitting only appeared for activated lattice beams.

By performing a horizontal line-cut which averages over 15 pixels in vertical direction through the middle of the image, the density distribution as shown in fig. 4.10 can be extracted. The sum of three Gauss distributions is fitted onto the normalized data giving numerical values for the centre position and the relative height of all three peaks.

The distance of both side peaks away from the center of the middle peak should depend on the momentum which is transferred to the atoms by the optical lattice beams. From this a theoretical value

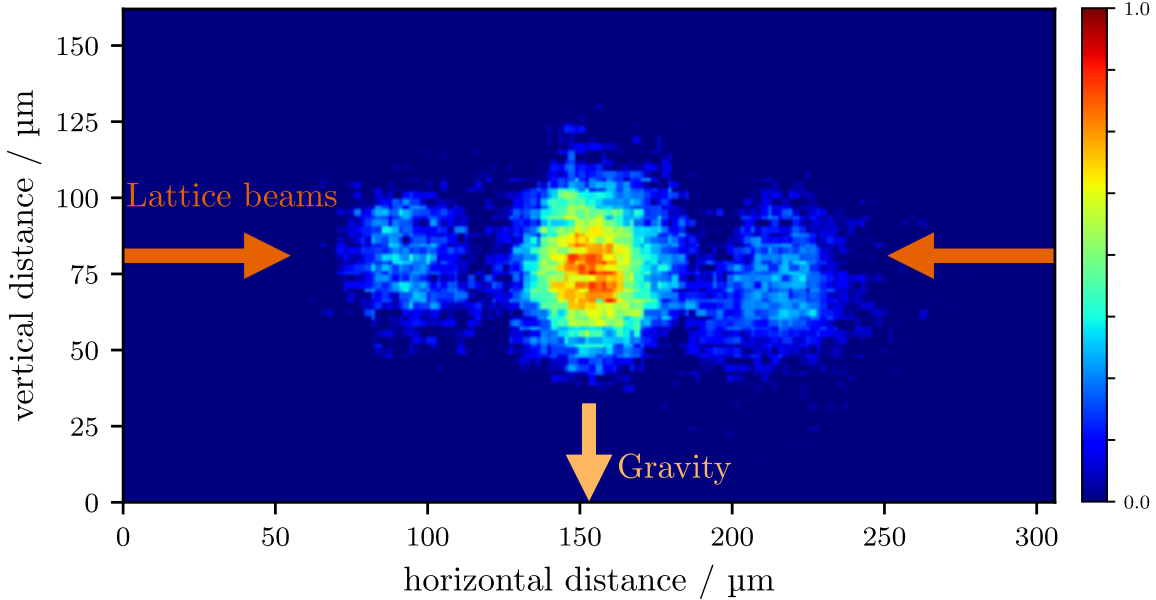


Figure 4.9: Absorption image of deflected BEC after a time of flight of 16 ms. Indicates the projected direction of the lattice beams and gravity. Image is not corrected for the observation angle of  $45^\circ$ .

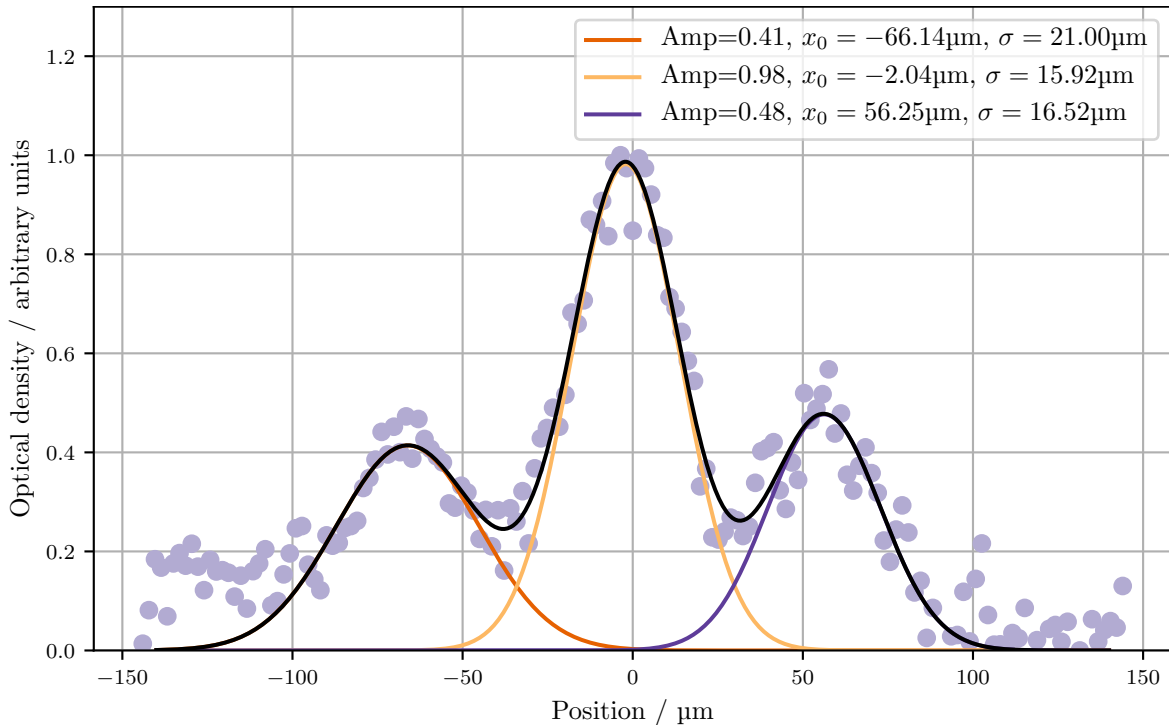


Figure 4.10: Line-cut through a single absorption image with Gaussian fits and extracted values.

for the mean velocity of the peaks is calculated as:

$$p = m \cdot v = 2\hbar k = \frac{2h}{\lambda} \quad (4.22)$$

$$\Rightarrow v_{\text{theo}} = \frac{2h}{\lambda m} \approx 5.65 \text{ mm s}^{-1} \quad (4.23)$$

The experimental value is obtained from

$$v_{\text{exp}} = \frac{d_{\text{meas}}}{\text{TOF}} \quad (4.24)$$

In section 2.3.7 the magnification factor to convert the distance in pixel into distance in meter is already introduced. At this point an additional correction factor is introduced, which takes into account that the separation of the cloud is observed under an angle of  $45^\circ$  instead of  $90^\circ$ . This leads to a projection onto the camera that is smaller than the actual separation. As indicated in fig. 4.11(b) for small angle  $\beta_l$  and  $\beta_r$  the adjustments to  $d_{\text{meas}}$ , resulting in the corrected value are calculated as:

$$d_{\text{cor}} = \frac{d_{\text{meas}}}{\cos(\alpha)} \approx 1.414 \cdot d_{\text{meas}} \quad \text{for } \alpha = 45^\circ \quad (4.25)$$

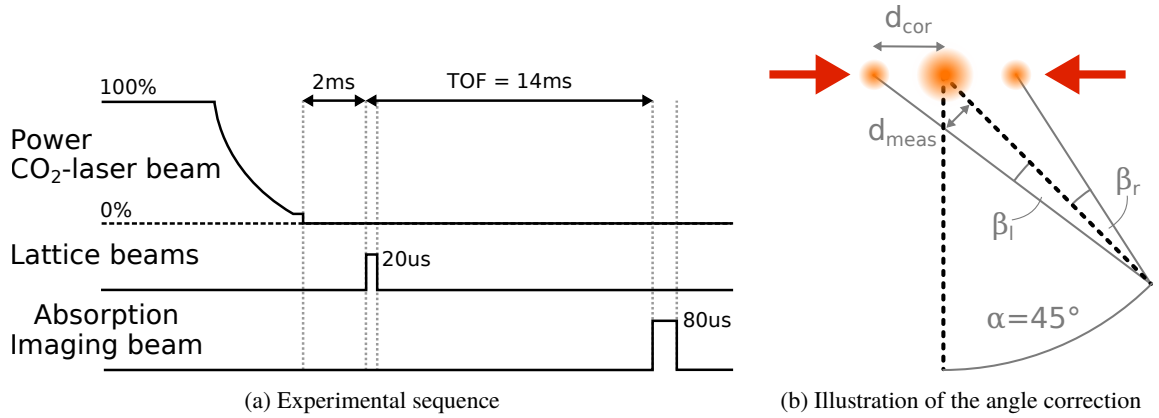


Figure 4.11: Illustration for the measurement process of the diffraction.

The calculated values resulting from the average over seven independent measurements with the same parameters follow as:

$$v_{\text{exp, left}} = (6.45 \pm 0.67) \text{ mm s}^{-1}$$

$$v_{\text{exp, right}} = (6.06 \pm 0.62) \text{ mm s}^{-1}$$

In fig. 4.12 all measurements are plotted individually, illustrating the distribution of data points over the measurement series. Even though the velocity for both side peaks should be equal, a difference is already observable in the line-cut image fig. 4.10, where the left peak does not only have a larger distance to the center but also shows a greater radius for every data set. This seems to be an indication for a distortion of the image due to the observation angle. Another systematic error which arises, is the angle of observation which, due to the optical set up and large chamber, can not be sufficiently

measured. It is extracted from the technical drawings of the chamber, assuming that the beam pass through the center of the windows. When assuming an angle of  $43^\circ$  instead, the measured values lie within one sigma of the measured values for the right side peak. Resulting from this a large error for the angle of about  $\Delta\alpha = \pm 2^\circ$  is assumed and together with the individual error of fits leads to the large uncertainty of the experimental values.

A precise determination of the angle between imaging system and lattice beams together with a consideration of the angles  $\beta$  or the relocation of the camera to a right angle observation should allow to overcome this uncertainty.

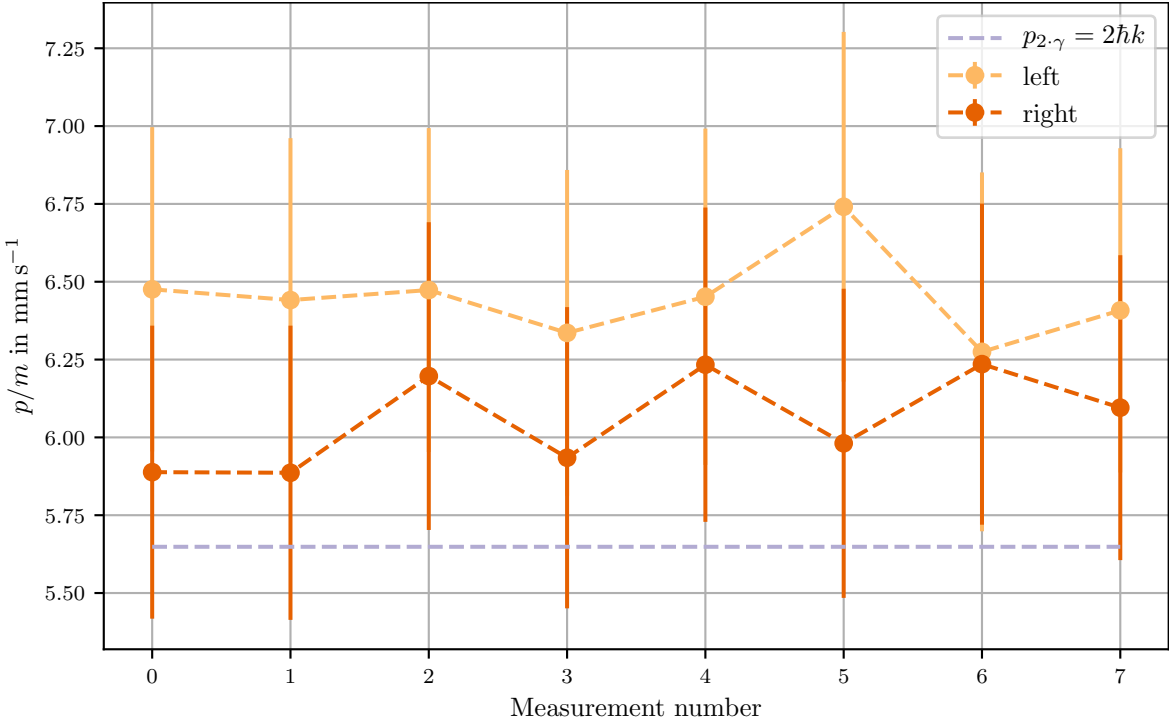


Figure 4.12: Calculated velocity of the side peaks visible in fig. 4.10 for different measurements. Calculated under the consideration of a  $45^\circ$  observation angle and assuming 14 ms TOF time. The dotted blue line indicates the theoretical expected value.

Another notable observation is the overlapping of the peaks which are not clearly separated as observed in other diffraction experiments. Resulting from the large mass and infrared wavelength of the lattice beams, the theoretical velocity for this experiment is about one magnitude smaller than for example in the early experiment by W. D. Phillips with Sodium [63] and other more current works [64, 69]. The radius of the side peaks in the order of  $17\text{ }\mu\text{m}$  compared to that of an observed BEC after the same TOF without any lattice beams activated (as for the radius inversion measurement in fig. 2.6). An improvement to separate the peaks more clearly would be a longer TOF duration. However this is not possible with the current imaging set-up since the observed signal-to-noise ratio for longer times becomes too small for a significant measurement. It should be possible to overcome this by a more sensitive imaging system and a higher atomic number in the initial condensate.

By the time of the measurement, the reference cavity lock of the used Ti:Sapphire laser was not

very stable. Thus, the used detuning can only approximately be determined and is in of the order of 100 MHz, corresponding to about  $10^4$  of the natural line-width of the used transition. It should be pointed out that the detuning could also have drifted to smaller (i.e. closer to resonant) values in part of the experimental runs. Given a subsequently occurring failure of the used commercial erbium oven shutter within the time limit available for this thesis work, no further measurements could be carried out. The current results clearly demonstrate Bragg scattering of erbium atoms with a standing wave tuned near to a narrow-line transition.

## CHAPTER 5

---

### Conclusion and Outlook

---

Ultracold erbium atoms are attractive systems for the far-off resonant manipulation of quantum gases with laser beams, which can allow for the observation of novel phases of matter, as bosonic fractional quantum Hall phases. In the course of this master thesis, the optical manipulation of erbium atoms with radiation tuned near a spectrally narrow inner-shell transitions was investigated.

To begin with a fluorescence spectroscopy was set up which has allowed to carry out the observation of spectra of the inner-shell transition near 841 nm wavelength for different erbium isotopes. It was possible to confirm the literature value for the Erbium isotope shifts at this wavelength. The realized set-up furthermore allows a fluorescence spectroscopy on the atomic beam for the two other visible wavelength in the laboratory, which is an useful tool for daily based troubleshooting when required.

In subsequent work an optical set-up for the Raman manipulation of ultracold erbium atoms was build up. With this set-up, Bragg diffraction of atoms from an erbium Bose-Einstein condensate has been observed in the course of this thesis. An first analyses on the relative velocity of atoms in the different diffraction orders has been realized and the observed value for the photon recoil for this transition agrees with expectations within experimental uncertainties.

In the near future, the measurements of the Bragg diffraction of atoms should be repeated with the lattice beams frequency stabilized by a new PID controller, which has also been realized as part of this work. The PID controller is part of a recently available wavemeter, offering a higher frequency accuracy of 30 MHz. This should allow for a corresponding reduction in the uncertainty of the lattice laser detuning from resonance.

Subsequently Doppler-sensitive Raman transitions could be implemented, which in the presence of an additional transverse gradient of the real magnetic field, should allow for the synthetisation of artificial magnetic fields for the cold erbium atoms. When implementing strong synthetic magnetic fields to two-dimensional erbium microclouds, this should lead the path to investigations of fractional quantum Hall physics in a well controlled neutral atomic system.



## Bibliography

---

- [1] A. Einstein, *Quantentheorie des einatomigen idealen Gases*, Preussische Akademie der Wissenschaft **261** (1924) (cit. on p. 1).
- [2] Bose, *Plancks Gesetz und Lichtquantenhypothese*, Zeitschrift für Physik **26** (1924) 178 (cit. on pp. 1, 3).
- [3] A. Einstein, *Quantentheorie des idealen einatomigen Gases, Zweite Abhandlung*, Sitzungsberichte der Preußischen Akademie der Wissenschaften, Physikalisch-Mathematische Klasse, Berlin (1925) 3 (cit. on p. 1).
- [4] K. B. Davis et al., *Bose-Einstein Condensation in a Gas of Sodium Atoms*, Phys. Rev. Lett. **75** (22 1995) 3969 (cit. on p. 1).
- [5] M. H. Anderson et al., *Observation of Bose-Einstein Condensation in a Dilute Atomic Vapor*, Science **269** (1995) 198, ISSN: 0036-8075 (cit. on pp. 1, 16).
- [6] C. C. Bradley et al., *Evidence of Bose-Einstein Condensation in an Atomic Gas with Attractive Interactions*, Phys. Rev. Lett. **75** (9 1995) 1687 (cit. on p. 1).
- [7] S. Stellmer et al., *Bose-Einstein Condensation of Strontium*, Phys. Rev. Lett. **103** (20 2009) 200401 (cit. on p. 1).
- [8] A. Griesmaier et al., *Bose-Einstein Condensation of Chromium*, Phys. Rev. Lett. **94** (16 2005) 160401 (cit. on p. 1).
- [9] S. Demokritov et al., *Bose-Einstein condensation of quasi-equilibrium magnons at room temperature under pumping*, Nature **443** (2006) 430 (cit. on p. 1).
- [10] J. Kasprzak et al., *Bose-Einstein condensation of exciton polaritons*, Nature **443** (2006) 409 (cit. on p. 1).
- [11] J. Klaers et al., *Bose-Einstein condensation of photons in an optical microcavity*, Nature **468** (2010) 545 (cit. on p. 1).
- [12] R. Grimm, M. Weidmüller and Y. B. Ovchinnikov, “Optical Dipole Traps for Neutral Atoms”, vol. 42, Advances In Atomic, Molecular, and Optical Physics, Academic Press, 2000 (cit. on pp. 1, 13).
- [13] Y. Takasu et al., *Spin-Singlet Bose-Einstein Condensation of Two-Electron Atoms*, Phys. Rev. Lett. **91** (4 2003) 040404 (cit. on p. 1).
- [14] K. Aikawa et al., *Bose-Einstein Condensation of Erbium*, Phys. Rev. Lett. **108** (21 2012) 210401 (cit. on p. 1).
- [15] S. Baier et al., *Realization of a Strongly Interacting Fermi Gas of Dipolar Atoms*, Phys. Rev. Lett. **121** (9 2018) 093602 (cit. on p. 1).

## Bibliography

---

- [16] A. Frisch et al., *Ultracold Dipolar Molecules Composed of Strongly Magnetic Atoms*, Phys. Rev. Lett. **115** (20 2015) 203201 (cit. on p. 1).
- [17] X. Cui et al., *Synthetic gauge field with highly magnetic lanthanide atoms*, Phys. Rev. A **88** (1 2013) 011601 (cit. on pp. 2, 5).
- [18] M. W. Zwierlein et al., *Vortices and superfluidity in a strongly interacting Fermi gas*, Nature **435** (2005) 1047 (cit. on p. 2).
- [19] V. Bretin et al., *Fast Rotation of a Bose-Einstein Condensate*, Phys. Rev. Lett. **92** (5 2004) 050403 (cit. on p. 2).
- [20] Y.-J. Lin et al., *Synthetic magnetic fields for ultracold neutral atoms*, Nature **462** (2009) 628, URL: <https://doi.org/10.1038/nature08609> (cit. on p. 2).
- [21] D. Babik et al., *Synthetic magnetic fields for cold erbium atoms*, 2019, arXiv: 1911.09583 [cond-mat.quant-gas] (cit. on pp. 2, 17).
- [22] J. Ulitzsch et al., *Bose-Einstein condensation of erbium atoms in a quasielectrostatic optical dipole trap*, Phys. Rev. A **95** (4 2017) 043614 (cit. on p. 2).
- [23] W. Pauli, *Über den Zusammenhang des Abschlusses der Elektronengruppen im Atom mit der Komplexstruktur der Spektren*, Zeitschrift für Physik A Hadrons and Nuclei **31** (1925) 765 (cit. on p. 3).
- [24] C. J. Pethick and H. Smith, *Bose-Einstein Condensation in Dilute Gases*, 2nd ed., Cambridge University Press, 2008 (cit. on pp. 3, 4, 24, 25).
- [25] F. Dalfovo et al., *Theory of Bose-Einstein condensation in trapped gases*, Reviews of Modern Physics **71** (1999) 463 (cit. on pp. 4, 13, 16).
- [26] P. C. Mosander, XXX. *On the new metals, lanthanum and didymium, which are associated with cerium; and on erbium and terbium, new metals associated with yttria*, The London, Edinburgh, and Dublin Philosophical Magazine and Journal of Science **23** (1843) 241 (cit. on p. 5).
- [27] A. F. Holleman and N. Wiberg, *Lehrbuch der Anorganischen Chemie*, de Gruyter, 2007 (cit. on p. 5).
- [28] J. Emsley, *Nature's building blocks: an AZ guide to the elements*, Oxford University Press, 2011 (cit. on p. 5).
- [29] J. Emsley, *The Elements (Oxford Chemistry Guides)*, vol. 3, Oxford University Press, 1998, ISBN: 978-0198558194 (cit. on p. 5).
- [30] R. J. Mears et al., *Low-noise erbium-doped fibre amplifier operating at 1.54μm*, Electronics Letters **23** (1987) 1026 (cit. on p. 5).
- [31] W. C. Martin, R. Zalubas and L. Hagan, *Atomic Energy Levels-The Rare-Earth Elements. The Spectra of Lanthanum, Cerium, Praseodymium, Neodymium, Promethium, Samarium, Europium, Gadolinium, Terbium, Dysprosium, Holmium, Erbium, Thulium, Ytterbium, and Lutetium*, tech. rep., NSRDS-NBS, Washington: National Bureau of Standards, U.S. Department of Commerce, 1978 (cit. on pp. 5, 6).

- 
- [32] J. E. Sansonetti and W. C. Martin, *Handbook of Basic Atomic Spectroscopic Data*, Journal of Physical and Chemical Reference Data **34** (2005) 1559 (cit. on p. 5).
  - [33] J. McClelland, *Natural linewidth of the 401-nm laser-cooling transition in Er I*, Phys. Rev. A **73** (2006) (cit. on p. 7).
  - [34] J. E. Lawler, J.-F. Wyart and E. A. Den Hartog, *Atomic transition probabilities of Er i*, Journal of Physics B Atomic Molecular Physics **43**, 235001 (2010) 235001 (cit. on p. 7).
  - [35] E. A. Den Hartog, J. P. Chisholm and J. E. Lawler, *Radiative lifetimes of neutral erbium*, Journal of Physics B Atomic Molecular Physics **43**, 155004 (2010) 155004 (cit. on p. 7).
  - [36] H. Y. Ban et al., *Laser cooling transitions in atomic erbium*, Opt. Express **13** (2005) 3185 (cit. on pp. 7, 17).
  - [37] J. Ulitzsch, *Erzeugung eines Bose-Einstein-Kondensats aus Erbiumatomen in einer quasi-elektrostatischen Dipolfalle*, PhD thesis: Rheinische Friedrich-Wilhelms-Universität Bonn, 2016 (cit. on pp. 7, 11, 13, 14, 16, 25).
  - [38] J. Schindler, *Characterization of an Erbium Atomic Beam*, MA thesis: University of Innsbruck, 2011 (cit. on p. 8).
  - [39] W. Demtröder, *Experimentalphysik 3: Atome, Moleküle und Festkörper*, Springer-Verlag, 2016, ISBN: 978-3-662-49093-8 (cit. on p. 9).
  - [40] H. Metcalf and P. van der Straten, *Laser Cooling and Trapping*, Graduate Texts in Contemporary Physics, Springer New York, 1999, ISBN: 0-387-98728-2 (cit. on pp. 9–13, 23).
  - [41] J. Dalibard and C. Cohen-Tannoudji, *Laser cooling below the Doppler limit by polarization gradients: simple theoretical models*, J. Opt. Soc. Am. B **6** (1989) 2023 (cit. on p. 10).
  - [42] N. Leefer et al., *Transverse laser cooling of a thermal atomic beam of dysprosium*, Phys. Rev. A **81** (4 2010) 043427 (cit. on p. 11).
  - [43] M. Rehberger, *Ultracold Erbium Atoms in Far-Detuned Optical Traps - Construction of a Zeeman-Slower*, MA thesis: Rheinischen Friedrich-Wilhelms-Universität Bonn, 2013 (cit. on pp. 11, 12).
  - [44] R. V. Roell, *Ultracold erbium atoms in a quasi-electrostatic optical dipole trap*, MA thesis: Rheinische Friedrich-Wilhelms-Universität Bonn, 2016 (cit. on pp. 13, 14).
  - [45] N. Masuhara et al., *Evaporative Cooling of Spin-Polarized Atomic Hydrogen*, Phys. Rev. Lett. **61** (8 1988) 935 (cit. on p. 14).
  - [46] W. Ketterle and N. V. Druten, “Evaporative Cooling of Trapped Atoms”, ed. by B. Bederson and H. Walther, vol. 37, Advances In Atomic, Molecular, and Optical Physics, Academic Press, 1996 181 (cit. on p. 14).
  - [47] A. McNelly, *Der neue internationale Atlas*, Westermann, 1997 (cit. on p. 15).
  - [48] N. Imagery and M. Agency, *Department of Defense World Geodetic System 1984: its definition and relationships with local geodetic systems*, 3rd ed., 1997 (cit. on p. 15).

## Bibliography

---

- [49] R. J. Lipert and S. C. Lee, *Isotope shifts and hyperfine structure of erbium, dysprosium, and gadolinium by atomic-beam diode-laser spectroscopy*, Applied Physics B **57** (1993) 373, ISSN: 1432-0649 (cit. on pp. 17, 21).
- [50] W. G. Jin et al., *Hyperfine Structure and Isotope Shift in Er I by the Atomic-Beam Laser Spectroscopy*, J. Phys. Soc. Jpn. **59** (1990) 3148 (cit. on p. 17).
- [51] W. Demtröder, *Laser spectroscopy 1: basic principles*, Springer, 2014, ISBN: 978-3-540-73415-4 (cit. on p. 17).
- [52] W. Demtröder, *Laser Spectroscopy, Basic Concepts and Instrumentation*, 3rd ed., Springer, 2002, ISBN: 3-540-65225-6 (cit. on p. 19).
- [53] J. Olivero and R. Longbothum, *Empirical fits to the Voigt line width: A brief review*, Journal of Quantitative Spectroscopy and Radiative Transfer **17** (1977) 233 (cit. on p. 19).
- [54] E. D. Black, *An introduction to Pound–Drever–Hall laser frequency stabilization*, American Journal of Physics **69** (2001) 79 (cit. on p. 22).
- [55] S. Altshuler, L. M. Frantz and R. Braunstein, *Reflection of Atoms from Standing Light Waves*, Phys. Rev. Lett. **17** (5 1966) 231 (cit. on p. 23).
- [56] A. Ashkin, *Atomic-Beam Deflection by Resonance-Radiation Pressure*, Phys. Rev. Lett. **25** (19 1970) 1321 (cit. on p. 23).
- [57] P. E. Moskowitz et al., *Diffraction of an Atomic Beam by Standing-Wave Radiation*, Phys. Rev. Lett. **51** (5 1983) 370 (cit. on p. 23).
- [58] P. Meystre, *Atom Optics*, Springer Series on Atomic, optical and plasma physics, Springer-Verlag, 2001, ISBN: 0-387-95274-8 (cit. on pp. 23, 26, 27).
- [59] M. Kozuma et al., *Coherent Splitting of Bose-Einstein Condensed Atoms with Optically Induced Bragg Diffraction*, Phys. Rev. Lett. **82** (5 1999) 871 (cit. on pp. 23, 26).
- [60] V. S. Letokhov, *Narrowing of the Doppler width in a Standing Light Wave*, JETP Lett. **7** (1968) 272 (cit. on p. 23).
- [61] O. Morsch and M. Oberthaler, *Dynamics of Bose-Einstein condensates in optical lattices*, Rev. Mod. Phys. **78** (1 2006) 179 (cit. on pp. 23–26).
- [62] M. Leder, *Quantensimulation von relativistischen Effekten mit ultrakalten Atomen in variablen optischen Gitterpotentialen*, PhD thesis: Rheinischen Friedrich-Wilhelms-Universität Bonn, 2016 (cit. on p. 23).
- [63] Y. B. Ovchinnikov et al., *Diffraction of a Released Bose-Einstein Condensate by a Pulsed Standing Light Wave*, Phys. Rev. Lett. **83** (2 1999) 284 (cit. on pp. 26, 35).
- [64] J. H. Huckans et al., *Quantum and classical dynamics of a Bose-Einstein condensate in a large-period optical lattice*, Phys. Rev. A **80** (4 2009) 043609 (cit. on pp. 27, 35).
- [65] D. Meschede, *Optik, Licht und Laser*, 2nd ed., Springer-Verlag, 2005, ISBN: 3-519-13248-6 (cit. on p. 28).
- [66] J. Noda, K. Okamoto and Y. Sasaki, *Polarization-maintaining fibers and their applications*, Journal of Lightwave Technology **4** (1986) 1071 (cit. on p. 28).

- 
- [67] J. M. Khosrofian and B. A. Garetz, *Measurement of a Gaussian laser beam diameter through the direct inversion of knife-edge data*, Appl. Opt. **22** (1983) 3406 (cit. on p. 30).
  - [68] Y. Suzaki and A. Tachibana, *Measurement of the  $\mu\text{m}$  sized radius of Gaussian laser beam using the scanning knife-edge*, Appl. Opt. **14** (1975) 2809 (cit. on p. 30).
  - [69] Y. Colombe et al., *Diffraction of a Bose-Einstein condensate in the time domain*, Phys. Rev. A **72** (6 2005) 061601 (cit. on p. 35).



# List of Figures

---

2.1	Erbium energy scheme . . . . .	6
2.2	Schematic overview of the whole set-up to create a BEC . . . . .	8
2.3	Effusion cell and transverse cooling set-up . . . . .	11
2.4	Schematic of the working principle of a MOT . . . . .	12
2.5	Imaging system calibration with accelerated BEC . . . . .	15
2.6	Aspect ratio inversion . . . . .	16
3.1	Set-up spectroscopy at TC . . . . .	20
3.2	Fluorescence signal near 841 nm . . . . .	21
3.3	Transversal cooling stage with spectroscopy set-up . . . . .	22
4.1	Illustration standing light wave . . . . .	24
4.2	Illustration of $2n$ -photon stimulated Raman transition . . . . .	27
4.3	Optical set-up for the preparation of the two lattice beams . . . . .	28
4.4	Setup of RF electronics for the switching of the lattice beams with an AOM . . . . .	29
4.5	Optical set-up of the lattice beams at the vacuum chamber . . . . .	30
4.6	Beamwaist of lattice beams at chamber . . . . .	30
4.7	Validation of the pulsduration and timing of the lattice beams . . . . .	31
4.8	Risetime measurement of lattice pulses behind optical fibers . . . . .	32
4.9	Absorption image of deflected BEC . . . . .	33
4.10	Fits onto image linecut of a deflected BEC . . . . .	33
4.11	Illustration for the measurement process of the diffraction . . . . .	34
4.12	Velocity of atomic side peaks . . . . .	35



## **List of Tables**

---

2.1	Characterization of all six stable atomic erbium isotopes . . . . .	5
2.2	Characteristic values for the used transitons in atom erbium . . . . .	7
4.1	Characteristic lattice properties at 840.990 nm . . . . .	25



## Acronyms

---

**AOM** acousto-optic modulator. 20, 22, 28, 29, 31, 32, 45

**BEC** Bose-Einstein condensate. 1–3, 7, 15, 16, 23, 25, 27, 32, 33, 35

**EOM** electro-optic modulator. 22

**FWHM** full width at half maximum. 18, 21

**LAN** local area network. 28

**MOT** magneto-optical trap. 10–13, 29, 30

**ODT** optical dipole trap. 13, 14

**PBS** polarizing beamsplitter. 28, 29, 31

**PMT** photomultiplier tube. 20–22

**RF** radio frequency. 28, 29, 31, 45

**RMS** root mean squared. 8

**TC** transversal cooling. 19–21, 45

**Ti:Sa** Titan:Saphir-Laser. 19, 20, 28, 37, 38

**TOF** time of flight. 14–16, 32, 35



# Danksagung

---

An erster Stelle möchte ich mich bei Prof. Dr. Weitz für die Möglichkeit bedanken, meine Masterarbeit in seiner Arbeitsgruppe zu absolvieren. Als Masterstudent hatte ich hier die Gelegenheit, an einem abwechslungsreichen und anspruchsvollen Experiment mitzuwirken, das nicht nur spannende physikalische Theorie, sondern auch selbständiges Arbeiten und Erforschen mit hochwertigen Instrumenten der (Quanten-) Optik ermöglicht hat. Durch seine Betreuung war ich aktiv in Entwicklungen eingebunden und bei täglichen Geprächen im Labor, in Gruppentreffen oder bei einer offenen Bürotür gab es immer Platz für Fragen und Diskussionen.

Prof. Dr. Simon Stellmar danke ich für die Übernahme der Zweitkorrektur. Die inspirierenden Gespräche über die Welt der Spektroskopie sowie die dabei stattfindende Führung durch eines seiner Experimente empfand ich als nicht selbstverständlich und hatte das Gefühl eines auf Forschungsgeist beruhenden, unkomplizierten Austauschs.

Besonderen Dank möchte ich Roberto aussprechen. Danke, dass ich von deiner großen Erfahrung mit dieser komplexen Maschine profitieren durfte. Danke dafür, dass du als Betreuer immer das Wohl und die Anerkennung deiner Schützlinge vor dein eigenes/eigene gestellt hast und danke für die Freundschaft und Unterstützung während der restlichen Stunden.

Danke an Johannes, der sich immer wieder in seiner eigenen Arbeit pausieren lassen hat, um mit Interesse und beeindruckendem Wissen jedwede Probleme zu unterstützen. Danke auch für die Inspiration an Hobbys und Bastelprojekten, vom Lautsprecherbau bis zum Schlosseröffnen.

Der gesamten Arbeitsgruppe möchte ich danken für die gute Zeit. Die experimentübergreifenden Gespräche zum Erarbeiten von Lösungen waren stets genauso bereichernd, wie die Ausgleich schaffenden Zeiten beim Essen, Kaffeetrinken, Sporttreiben oder sonstigen Freizeitaktivitäten. Wie oft man am Wochenende oder zu nächtlichen Arbeitszeiten noch jemanden von euch antraf und sich gemeinsam unterstützte, ist beeindruckend.

Dr. Frank Vewingers Büro ist für viele Menschen im Institut eine Anlaufstelle für Fragestellungen bei denen man selbst keine zufriedenstellende Antwort findet und für die er meist eine dann scheinbar triviale Antwort parat hat - danke dafür.

Meinen Eltern möchte ich an dieser Stelle danken für die Unterstützung während meines gesamten Studiums, dass sie zu jeder Zeit hinter mir stehen und einen großen Teil dazu beigetragen haben wer ich heute bin.